IEEE Access
Multidisciplinary | Rapid Review | Open Access Journal

SPECIAL SECTION ON EMERGING TRENDS, ISSUES AND CHALLENGES FOR ARRAY SIGNAL PROCESSING AND ITS APPLICATIONS IN SMART CITY

Received June 11, 2019, accepted June 24, 2019, date of publication July 24, 2019, date of current version August 9, 2019.

Digital Object Identifier 10.1109/ACCESS.2019.2930746

Impact of Overlapped AoAs on the Achievable Uplink Rate of Hybrid Beamforming for Massive MIMO mm-Wave Systems for Industrial Environments

OSAMA ALLUHAIBI, (Member, IEEE), ERIK KAMPERT, PAUL A. JENNINGS, AND MATTHEW D. HIGGINS, (Senior Member, IEEE)
WMG, The University of Warwick, Coventry CV4 7AL, U.K.

Corresponding author: Osama Alluhaibi (o.alluhaibi@warwick.ac.uk)

This work was supported in part by the WMG Centre High Value Manufacturing Catapult, The University of Warwick, Coventry, U.K., and in part by the EPSRC through the UK-RAS network.

ABSTRACT In this paper, we develop novel precoder and combiner schemes for multi-user hybrid digital-to-analog (D-A) beamforming for uplink massive multiple-input multiple-output millimeter wave (mm-Wave) systems, where the number of radio frequency chains is much smaller than the number of antennas each transceiver is equipped with. Industry 4.0 targets to accelerate the digitalization of manufacturing processes by allocating fixed and mobile robotics which use wireless communication. Such development requires high data throughput for which the utilization of short distance wireless communication such as mm-Wave system is crucially required. Based on our measurements, the probability of mm-Wave propagation waves to be reflected and refracted from metallic surfaces are shown to be significantly high. Consequently, uplink transmissions from different users such as robotics, machines, and sensors can go through paths sharing the same physical scatters, some transmission paths of different users may have overlapped angle of arrivals (AoAs) at the base station. Under such circumstance, the correlation between the channel vectors also increases considerably, which affects the achievable uplink rate severely. Therefore, the intrinsic focus is on substantially maximizing the desired signal while reducing the system interference. The proposed analog precoders and combiners are designed by using the power iteration and the Riemannian optimization method based on Stiefel manifold algorithms, respectively. The proposed digital combiner adapts the minimum mean-square error by judiciously exploiting the effective uplink analog channel gains. Furthermore, the channel estimation is investigated through a newly designed two-step procedure. In each scattering point, there is the strongest power point which is detected and then used to improve the accuracy by employing an angular domain scheme. The impact of this paper will be the boosting of the achievable uplink rate in industrial environments.

INDEX TERMS Hybrid precoding and combining, millimetre wave, massive MIMO, Riemannian manifold optimization problem.

I. INTRODUCTION

The prevalence of increasing numbers of wireless smart devices has generated a continuing demand for an increase of reliable wireless data throughput. One solution for substantially increasing the data throughput in the future wireless communications is to combine millimetre-wave (mm-Wave) bands (frequency ranges from 6 GHz to 300 GHz) [1]–[3] with massive multiple-input multiple-output (MIMO) [4]–[6]. Fundamentally, in MIMO systems, the number of radio frequency (RF) chains is equal to the number of antennas, so the highest performance gain is achieved by using a fully digital precoder scheme. However, the associated large number of RF chains will have extremely high power consumption, and the hardware complexity will also increase dramatically [2], [6]–[8]. Therefore, a hybrid

The associate editor coordinating the review of this manuscript and approving it for publication was Liangtian Wan.

digital-to-analog (D-A) precoding and combining system has been proposed to balance the achievable rate, power consumption, and the implementation complexity [7]–[12]. Fundamentally, the hybrid D-A structure consists of a small-number of RF chains, called the digital part, and a large-number of antennas, called the analog part. Hence, the optimal hybrid D-A precoding and combining design is an intractable non-convex constant modulus constraint optimization problem [7]–[12].

It has been demonstrated in recent research that the rough surfaces of buildings and the rifts between small buildings can cause diffused scattering in mm-Wave channels [1]–[3]. In urban areas (i.e., factories, shopping malls, stadiums, smart city centers), the number of unforeseen scatters increases considerably so that mm-Wave signal channels may not have isolated angles of arrivals (AoAs) at the base station (BS). Measurements to study the AoAs of the propagation signals [13] in Daejeon City, Korea, showed that the propagation paths of multiple users were observed to pass through the non-negligible common scatterers, thus the arrived signals tended to overlap at the BS.

To understand the implications of an industrial environment on a mm-Wave communication channel, we have performed channel measurements in the industrial setting of the Warwick Manufacturing Group (WMG) Engineering Workshop. The WMG workshop has a large number of metallic surfaces machines, and fixed robotics. A typical resulting power delay profile will show the existence of common scatters and overlapped AoAs in mm-Wave channels where industrial scenarios are considered. This affects the achievable uplink rate of hybrid beamforming for massive MIMO mm-Wave systems.

A. RELATED WORK

For the multi-user scenario, various hybrid D-A precoding and combining schemes have been proposed [9]–[12]. For instance, a hybrid D-A system was designed by considering the weighted sum mean square error (WSMSE) based on the theory of compressed sensing in [9]. To reduce the number of RF chains, the precoder and combiner problem are proposed to split into two stages [10]. In stage one, a beamsteering based algorithm was proposed for the analog part and in stage two, a zero-forcing (ZF) solution was developed for the digital part [10]. Though simple, such a system sacrifices the achievable rate when a realistic multipath channel is applied to it. To resolve this issue, maximum ratio combining (MRC) was proposed to design the analog precoding and then ZF was applied for the digital precoding [11]. However, MRC [11] did not consider the effects of large interference in the system which consequently reduces the achievable rate. In [12], the analog precoding was designed by using the extended version of the conventional orthogonal matching pursuit (OMP) and the digital precoding was designed based on minimum mean-square error (MMSE). The elements of analog precoding and combining matrices were selected from a pre-defined dictionary which depends on AoAs and angles of departures (AoDs) [12]. However, in massive MIMO mm-Wave systems with high user density, there is a noticeable achievable rate gap between the hybrid D-A based on OMP and the fully digital system [12]. According to [14] the AoAs and AoDs of the paths in the mm-Wave channel can be grouped in several separated spatial lobes where in each different group they are sufficiently separable, whereas the AoAs and the AoDs of the paths in one spatial lobe are relatively close. Based on this, authors in [15], [16] exploited this sparseness property in the angular domain to divide the mm-Wave channel approximately orthogonally, which has been used to reduce the complexity of the hybrid precoding and improve the system performance.

The majority of contributions in the literature [9]–[12], [14]–[16] have assumed that the propagation paths corresponding to different users have independent channel vectors which results in non-overlapping AoAs at the BS. From the previous two different measurements, there is a high probability that some propagation paths of multiple users[1] will share some common scatterers in dense urban areas [13], [17], therefore these different propagation paths will have the same AoAs at the BS which generate a severe interference in the system. Undoubtedly, with the hybrid D-A massive MIMO mm-Wave system, this type of interference cannot be eliminated by the digital processing domain only, which is restricted to fewer RF chains. In this case, if the existing precoders and combiners [9]–[12] are applied directly, it will induce significant achievable rate loss in the hybrid D-A massive MIMO mm-Wave systems. Hence, it is of paramount importance that such system should be designed carefully.

In [17] the authors developed an algorithm to handle the interference due to signals with overlapped AoAs at the BS. Initially the Gram-Schmidt (GS) algorithm is formed for the analog part and then the MMSE scheme is applied at the digital part. However, in GS, the vector is updated iteratively and finally these vectors do not completely eradicate the interference at the analog stage. As a result, this incurs in a large performance gap away from the fully digital system. Authors in [18] have proposed iterative hybrid precoding based on OMP algorithm and have discussed the interference of overlapped AoAs based on the assumption that the hybrid precoding and combining already existed as codebook tables. The idea in [18] is to divide the codebook tables into a precoder table and combiner table. And then use the OMP algorithm to search between the codebooks for the precoder and combiner pair that can provide a maximum gain. This step basically depends on an exhaustive search method, after which the pair that achieves maximum gain is removed from the codebook table to avoid an extra-interference. This idea functions well when the correlation between the table pairs is low, and when a small number of codebooks exist in order to search and respond quickly enough. However, in industry 4.0 measurements, the number of mm-Wave prop-

[1]Note that, in this paper robotics, machines, and mobiles have been called users.

agation waves that are reflected and refracted from metallic surfaces are shown to be significantly high which consequently increases the correlation between users. In addition, the algorithms developed in [9]–[12], [17] are only applicable for multiple-input single-output (MISO) systems, where each user is equipped with a single antenna.

Channel estimation for hybrid D-A massive MIMO mm-Wave systems is crucial. The main challenges arise from the digital part estimator being positioned behind the analog part. This only provides the digital part with access to the effective analog channel gains with lower dimensionality. This limitation motivated researchers to develop new channel estimation algorithms. A promising scheme based on compressed sensing theory [19] was proposed, which relies heavily on the sparsity property of the mm-Wave channels. However, this algorithm is not feasible when there is considerable scattering in mm-Wave channels. To overcome the previous drawbacks, a Hierarchical Beamforming Training algorithm (HBT) was designed in [20] recently. To estimate the channel angles, HBT begins with dividing the full estimated angle spaces, number of sectors, and number of antennas into hierarchical levels. The main constraint is that the number of estimated angles and sectors must double that of the corresponding number of antennas at each level. As the number of sectors increases linearly, HBT suffers severely from the sectors' overlapped interference problem which also affects the accuracy of choosing the estimated angles.

B. CONTRIBUTION

The existing research has assumed the non-overlapped AoAs case, or that there are no precise beamformers designed to decrease the overlapped AoAs interference. However, our measurements in industrial environments will show that there are common scatters clustered, i.e., that there are overlapped AoA scenarios. Hence, the current estimation channel algorithms are neither practical in industrial scenarios with lots of scatters, nor do they estimate accurate angles due to overlapped sectors' interference. Therefore, the primary target of this paper is to maximize the desired channel gain while mitigating the interference that originates from the signals through some common scatters. To this end, a low dimension matrix based on combining all the precoders, channels, and combiners is formulated and called effective uplink analog channel gains. In this matrix, the diagonal elements represent the desired channel gains and the off-diagonal elements denote the interferences of the system. Finally, a method is proposed that can estimate the mm-Wave channels more accurately in the common scatters scenarios. The contributions of this paper are summarized as follows:

1) Channel sounding measurements focusing on the 28 GHz band in an existing modular factory will provide a detailed understanding of the typical behavior of mmWave signals in such an environment. This will support further description of practical statistical channel models, specifically for the industry vertical, needed by standardization bodies like 3GPP [21] due to the current known limitations in the existing mmWave models for indoor, outdoor and other vertical environments. Further, the channel sounding measurements at 28 GHz in a manufacturing setting display the scattering-rich characteristics of mm-Wave propagation in industrial environments.
2) The analog precoder is designed by utilizing a Power Iteration (PI) algorithm. This algorithm works by calculating the eigenvector that corresponds to the largest eigenvalue of a matrix. PI exploits the availability of the channel knowledge to the users in order to design the analog precoder. To satisfy the non-convex constant modulus constraint, the phases of the eigenvector are extracted that correspond to the largest eigenvalue which is optimally found by PI. Conceptually, this algorithm is similar to the optimal SVD operation, but avoids its high complexity especially for large matrices. Moreover, in this paper a modified version is proposed that avoids previous convergence problems.
3) The analog combiner at the BS needs to be maximizing the received power of the desired signal while suppressing the impacts of off-diagonal elements. This is achieved through using a Riemannian optimization method based on Stiefel manifold (ROSt) under orthogonal constraints. The non-convex constant modulus constraints are ignored in the first steps until the optimal solution is found, based on the cost function by using ROSt. In the final step, the analog combiner will extract the phase of the optimal solution in order to satisfy the constant modulus constraint. In contrast to [9], [10], [12], our proposed approach aims to directly optimize the achievable uplink rate of the hybrid D-A massive MIMO mm-Wave system when optimizing the analog combiners. The other advantage of the proposed ROSt is that it removes the need for any pre-defined candidate set for the analog part (e.g. OMP).
4) In order to further improve the achievable uplink rate, the interference in the effective uplink analog channel gains is further reduced. The digital combiner will be designed jointly by exercising MMSE based on uplink analog channel gains.
5) We propose a two-step multi-user channel estimation scheme for mm-Wave channels. In the first step, the strongest power scatterer point in the scenario is detected, instead of estimating jointly all the combination of multiple paths and angles as in [20]. In the second step, a search method based on an angular domain is proposed which aims to search for the strongest points for all the paths. This step allows our proposed estimation method to avoid the drawback of lacking channel estimation accuracy, as in [20] where the accuracy suffered from the sectors' overlapped interference problem.

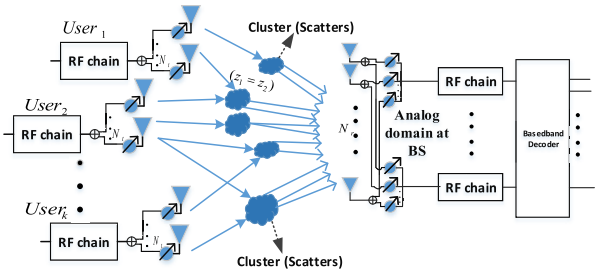

FIGURE 1. Diagram of K users that apply only analog precoding simultaneously transmit to a BS using a hybrid D-A combiner massive MIMO mm-Wave system.

Simulation results will show that the proposed PI and ROSt algorithms can outperform the existing algorithms [9]–[12], [17] in terms of achievable uplink rate. Finally, the proposed estimation method attains a lower channel estimation error than HBT [20].

Notation: Bold uppercase letter $\boldsymbol{X}$, and lowercase letter, $\boldsymbol{x}$, denote matrices and vectors, respectively. The transpose and conjugate transpose of a matrix are denoted by $(\cdot)^T$ and $(\cdot)^H$ respectively. $||\cdot||_F$ denotes Frobenius norm of a matrix, while $||\cdot||_1$ and $||\cdot||_2$ denote the 1-and 2-norm of a vector. The diagonal matrix is denoted as diag$[\cdot]$, and $\nabla f(\boldsymbol{X})$ denotes the classical gradient of f seen as a function in an Euclidean space.

II. UPLINK MODEL

Consider a single cell uplink multi-user hybrid D-A massive MIMO mm-Wave system as illustrated in Fig. 1. A BS is equipped with a large-scale antenna array of N_r antennas and N_{RF} RF chains, where each RF chain is connected to all N_r antennas. It is assumed that the BS communicates with K users, each of which has N_t antennas and one single RF chain. Therefore, each user can transmit one data stream at one time. It is assumed $K \leq N_{RF}$ in the system. K users are allowed to share the same spectrum. Then, the received signal at the BS is given by

$$\boldsymbol{y}_{\text{ul}} = \sum_{k=1}^{K} \boldsymbol{H}_k \boldsymbol{j}_{RF_k} s_k + \boldsymbol{n}, \tag{1}$$

where the matrix $\boldsymbol{H}_k \in \mathbb{C}^{N_r \times N_t}$ represents the uplink channel for the user k and s_k is the transmitted data symbol of the user k. $\boldsymbol{j}_{RF_k}$ is the analog precoder which is implemented by analog components like phase shifters, i.e., an $N_t \times 1$ vector with constant modulus entries. $\boldsymbol{n}$ is the noise vector that follows $\boldsymbol{n} \sim \mathcal{CN}(\boldsymbol{0}, \sigma^2 \boldsymbol{I}_{N_r \times 1})$. It is assumed that the data symbols for users are independent and with unit power, i.e., $\mathbb{E}[s_k s_i] = 0, k \neq i$, and $\mathbb{E}[|s_k|^2] = 1$. For data-transmission, beamforming is implemented at the BS to decode the users' data streams. Specifically, at the BS, by using combining vector $\boldsymbol{g}_k$ to decode user k's signal, we have

$$\boldsymbol{g}_k^H \boldsymbol{y}_{\text{ul}} = \boldsymbol{g}_k^H \boldsymbol{H}_k \boldsymbol{j}_{RF_k} s_k + \boldsymbol{g}_k^H \sum_{i \neq k} \boldsymbol{H}_i \boldsymbol{j}_{RF_i} s_i + \boldsymbol{g}_k^H \boldsymbol{n}, \tag{2}$$

where $\boldsymbol{g}_k = \boldsymbol{A}\,\boldsymbol{d}_k \in \mathbb{C}^{N_r \times 1}$ denotes the hybrid D-A combiner at the BS. The analog combiner matrix at the BS is denoted as $\boldsymbol{A} = [\boldsymbol{a}_1, \ldots, \boldsymbol{a}_{N_{RF}}] \in \mathbb{C}^{N_r \times N_{RF}}$, where $\boldsymbol{a}_i \in \mathbb{C}^{N_r \times 1}$, is a phase array of adjustable phase shifters connected to the ith RF chain. In other words, each analog combiner $\boldsymbol{a}_i$ has the same amplitude but different phase shifters. The data symbol will be further separated by applying an $N_{RF} \times K$ digital combiner (without the constant modulus constraint on its elements) $\boldsymbol{D} = [\boldsymbol{d}_1, \ldots, \boldsymbol{d}_K] \in \mathbb{C}^{N_{RF} \times K}$, where $\boldsymbol{d}_k \in \mathbb{C}^{N_{RF} \times 1}$.

A. CHANNEL MODEL

The mm-Wave channel can be portrayed with the popular multipath channel model [1], [3], [22], in which a number of propagation paths are associated with a few scatterer points. To consolidate this phenomenon, in this paper the extended 3-dimensional (3D) Saleh-Valenzuela geometry-statistical model is adopted [22]. The channel of user k can be written as

$$\boldsymbol{H}_k = \frac{1}{\sqrt{N_{cl}}} \sum_{m=1}^{N_{cl}} \sqrt{c_{km}}\, \boldsymbol{H}_{km}, \tag{3}$$

where $\boldsymbol{H}_{km}$ denotes the 3D mm-Wave channel from user k to the BS via cluster m. In general, when the signals hit an object (e.g., metallic surfaces, walls), this phenomenon will create l paths from a few physical scatters close to each other forming a cluster. Therefore, in such case where the number of scatters has a significantly large physical size, it is meaningful to contemplate the entire scatter as common scatters for different l paths and different users as shown in Fig. 2. Extraordinarily, for shorter wavelengths, it is possible to have l paths from each scatter point. However, mm-Wave channel measurements [1], [3], [22] showed that most of these paths carry a very low power which can be ignored and the dominant power is concentrated merely on one or two paths, thus each scatter point produces one path in this work. Even though, it can be also observed from Fig. 2 that there is still an autonomous lth path which is represented as uncommon path. In $\boldsymbol{H}_k$, the total number of clusters is denoted as N_{cl}. c_{km} denotes the significance of cluster m for user k, which measures the percentage of energy carried by cluster m with $\sum_{m=1}^{N_{cl}} c_{km} = N_{cl}$ [22]. $\boldsymbol{H}_{km}$ is represented as

$$\boldsymbol{H}_{km} = \sqrt{\frac{N_t N_r}{L_{km}}} \sum_{l=1}^{L_{km}} e^{j\Delta_{kz_{l_{km}}}} h^{3D}_{z_{l_{km}}} \boldsymbol{s}\boldsymbol{v}_r(\theta^r_{z_{l_{km}}}, \phi^r_{z_{l_{km}}}) \boldsymbol{s}\boldsymbol{v}^H_t(\theta^t_{z_{l_{km}}}, \phi^t_{z_{l_{km}}}), \tag{4}$$

where $\mathbb{L}_{km} = [1, \ldots, L_{km}]$ is the propagation paths index set of user k from cluster m. $\Delta_{kz_{l_{km}}} \in [-\pi/2, \pi/2]$ is the uniformly distributed random phase for l_{km} propagation path and cluster m. $h^{3D}_{z_{l_{km}}}$ is independent and identically distributed (i.i.d) $\mathcal{CN}(0, \delta_k^2)$ random variables with δ_k^2 representing the user k data channel's propagation attenuation. The scatter index set is denoted as $\mathbb{Z}$ where $z_{l_{km}} \in \mathbb{Z}(\forall l_{km} \in \mathbb{L}_{km})$ represents the scatter index of l_{km} paths. $\theta^r_{z_{l_{km}}}(\phi^r_{z_{l_{km}}})$ and $\theta^t_{z_{l_{km}}}(\phi^t_{z_{l_{km}}})$ represent the zenith (azimuth) AoA and

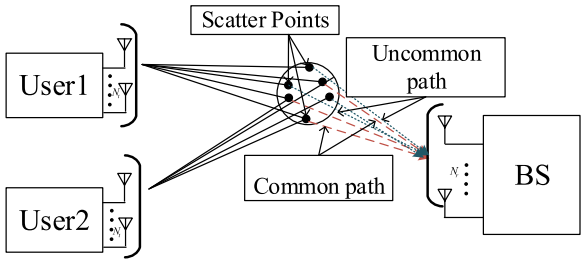

FIGURE 2. Example of a scenario with two users transmitting to the BS through common scatter points.

AoD, respectively. As the uniform planar antenna (UPA) structure [8] is a preferred choice for a 3D channel, in this case, $N_t = N_{t_x} \times N_{t_y}$, and $N_r = N_{r_x} \times N_{r_y}$, where (N_{t_x}, N_{r_x}) and (N_{t_y}, N_{r_y}) represent the numbers of antennas in the x-axis and y-axis. In the following notation, the superscript (or subscript) t and r are used to represent transmitter and receiver, respectively. $\boldsymbol{sv}_b(\theta^b_{zl_{km}}, \phi^b_{zl_{km}})$ in (4) represent the normalized receive and transmit array response vectors associated with AoA and AoD, where $b \in \{r, t\}$ represents arrival at the receiver (r) or departure at the transmitter (t), is given by [7], [8]

$$\boldsymbol{sv}_b(\theta^b_{zl_{km}}, \phi^b_{zl_{km}}) = \text{vec}[\boldsymbol{sv}_{b_x}(\Psi)\boldsymbol{sv}^H_{b_y}(\Phi)], \quad b \in [r, t], \quad (5)$$

where the directions of the array responses $\boldsymbol{sv}_{b_x}$ and $\boldsymbol{sv}_{b_y}$ are represented by $\boldsymbol{sv}_{b_q}$ and devised as

$$\boldsymbol{sv}_{b_q}(\Omega) = \frac{1}{\sqrt{N_{b_q}}}\left[1, e^{j\Omega}, \ldots, e^{j(N_{b_q}-1)\Omega}\right]^T, \quad q \in [x, y], \quad (6)$$

where $\Omega \in \{\Psi, \Phi\}$ are the values of Ψ and Φ that are given by

$$\begin{aligned} \Psi &= -2\pi\lambda^{-1}u_x \sin(\theta^b_{zl_{km}})\cos(\phi^b_{zl_{km}}), \\ \Phi &= -2\pi\lambda^{-1}u_y \sin(\theta^b_{zl_{km}})\sin(\theta^b_{zl_{km}}), \end{aligned} \quad (7)$$

where λ is the wavelength, and u_x and u_y are the inter-element distances in the x-axis and y-axis, respectively.

B. MM-WAVE CHANNEL MEASUREMENT IN INDUSTRIAL ENVIRONMENTS

In order to understand the implications of an industrial environment on a mm-Wave communication channel, we have performed channel measurements in the industrial setting of the WMG engineering workshop. This workshop is comparable to an industrial environment. As shown in the inset of Fig. 3, the workshop has a large number of metallic surfaces, machines and fixed robotics for designing automotive components.

A directional horn antenna with a half-power beam width of 10° was used as a transmitter on top of an eight meter high bridge overlooking the workshop floor. An omnidirectional antenna with an elevation half-power beam width of 20° was used as a receiver, mounted on a mobile trolley, one meter above the workshop floor. The former ensured a powerful beam, enabling possible line-of-sight (LoS) signals with strengths far above the receiver's noise threshold,

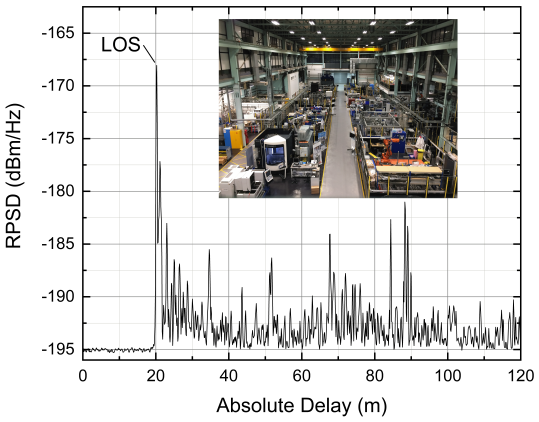

FIGURE 3. Typical power delay profile for the 28 GHz mm-Wave channel in the WMG engineering workshop (inset).

whereas the latter allowed for the detection of multipath components (MPCs) from any possible direction, due to reflections from the metallic industrial environment. For various locations of both transmitter and receiver, the antennas were manually boresight aligned before a channel measurement was started. Our channel sounding equipment used the pulse compression method of an R&S SMW200A Vector Signal Generator for the transmission of a frequency band limited signal with a carrier frequency of 28.5 GHz and an arbitrary modulated waveform with a clock frequency up to 2.4 GHz. An R&S FSW85 Signal and Spectrum Analyzer and an R&S RTO2044 Digital Oscilloscope were used for the processing of the received signals with a maximum sampling rate of 2.4 GHz. Further details on our channel sounding procedure can be found in our previous work [23]. A typical resulting power delay profile is displayed in Fig. 3, with the received power spectral density (RPSD) versus the absolute time delay between transmitted and received signal converted into meters. The first observed signal is the LoS peak at 20 m, which is the transmitter-receiver distance for this particular measurement. The LoS signal is followed by several MPCs with reduced RPSD values, some common scatters are clustered together potentially due to reflections from the same larger object within the 70 × 30 m workshop area. When taking into account a noise detection threshold of −190 dBm/Hz, the last strong cluster of MPCs is visible at an absolute delay of 90 m, resulting in an overall root mean square delay spread of 100 ns. The experiment, described here, was conducted in order to show the existence of common scatters and overlapped AoAs in mm-Wave channels where industrial scenarios were considered. This phenomenon affects the achievable uplink performance rate of such systems.

C. CASES OF COMMON SCATTERS (OVERLAPPED AOA) ON THE PROPAGATION SIGNAL

It has been substantiated that in mm-Wave channels (short distance propagation), the rough surfaces of buildings, small building rifts, a large number of metallic surfaces, machines

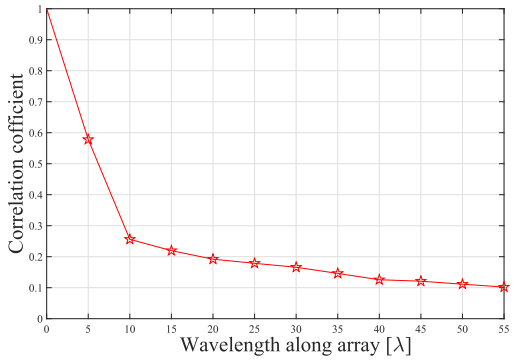

FIGURE 4. Comparison of the averaged spatial auto-correlation comparison between the channel of different users.

and fixed robots can cause diffused scattering, and considerable attenuation with decreasing wavelength [1], [3]. Fig. 4 confirms that the wavelength λ has a great impact on increasing the correlation between the channels of different users. Fundamentally, for mm-Wave frequencies λ is small compared to λ for low frequencies, thus from Fig. 4 it can be seen that the correlation of the mm-Wave system is high, which affects the achievable uplink rate performance directly. Therefore, utilizing mm-Wave communications in a dense area (i.e., industries, shopping malls, stadiums, city centers) will cause multiple user paths to share the same scatters. For these scenarios, different cases need to be investigated in multi-user hybrid D-A massive MIMO mm-Wave systems. First, the extreme case, when all the paths of several users share the same common scatters which arrive with completely overlapped AoAs at the BS. Second, the most likely case, when some of the propagation paths are overlapped which are easily spotted when two users share some of the common scatters, i.e., there exist at least two paths $l_1 \in \mathbb{L}_{k_1}, l_2 \in \mathbb{L}_{k_2}$ sharing the same common scatters points $z_1 = z_2$. Third, the perfect case, when several users paths arrive with non-overlapped AoAs at the BS. Our main analysis in this section is stated in Lemma 1.

Lemma 1: By using $\boldsymbol{sv}_b(\theta^b_{z_{lkm}}, \phi^b_{z_{lkm}})$ (as in (4)), and assuming an UPA structure, the array responses of different users propagated through common scatters then have the following result:

$$\boldsymbol{sv}_b^H(\theta_1^b,\phi_1^b)\boldsymbol{sv}_b(\theta_2^b,\phi_2^b),$$
$$\begin{cases} =1, & if\,(\theta_1^b=\theta_2^b)\ and\ (\phi_1^b=\phi_2^b) \\ =v_2(\theta_1^b,\phi_1^b,\theta_2^b,\phi_2^b), & \begin{bmatrix} if\,(\theta_1^b\neq\theta_2^b), and(\phi_1^b=\phi_2^b) \\ if(\theta_1^b=\theta_2^b) and(\phi_1^b\neq\phi_2^b) \end{bmatrix}, \\ =v_1(\theta_1^b,\theta_2^b)v_2(\theta_1^b,\phi_1^b,\theta_2^b,\phi_2^b), & \text{else} \end{cases}$$

where $v_2(\theta_1^b,\phi_1^b,\theta_2^b,\phi_2^b) = \left[\frac{1-e^{jkdn_{b_x}(\sin(\theta_1^b)\sin(\phi_1^b)-\sin(\theta_2^b)\sin(\phi_2^b))}}{1-e^{jkd(\sin(\theta_1^b)\sin(\phi_1^b)-\sin(\theta_2^b)\sin(\phi_2^b))}}\right]$, and $v_1(\theta_1^b,\theta_2^b) = \left[\frac{1-e^{jkdn_{b_y}(\cos(\phi_1^b)-\cos(\phi_2^b)}}{1-e^{jkd(\cos(\phi_1^b)-\cos(\phi_2^b)}}\right]$. For simplicity and making the analysis clear, the number of paths and shared scatters is assumed to be equal to one, where (θ_1^b,ϕ_1^b) and (θ_2^b,ϕ_2^b) are angles for two different users, respectively.

[***Proof***:] From (4), we have

$$\begin{aligned}
&\boldsymbol{sv}_b^H(\theta_1^b,\phi_1^b)\boldsymbol{sv}_b(\theta_2^b,\phi_2^b),\\
&=\frac{1}{N_b}\sum_{n_{b_x}=1}^{N_{b_x}}\sum_{n_{b_y}=1}^{N_{b_y}} e^{jkd(n_{b_x}-1)(\cos(\theta_1^b)-\cos(\theta_2^b))}\\
&\quad\times e^{jkd(n_{b_y}-1)(\sin(\theta_1^b)\sin(\phi_1^b)-\sin(\theta_2^b)\sin(\phi_2^b))}\\
&=\frac{1}{N_b}\left[\sum_{n_{b_x}=1}^{N_{b_x}} e^{jkd(n_{b_x}-1)(\cos(\theta_1^b)-\cos(\theta_2^b))}\right]\\
&\quad\times\left[\sum_{n_{b_y}=1}^{N_{b_y}} e^{jkd(n_{b_y}-1)(\sin(\theta_1^b)\sin(\phi_1^b)-\sin(\theta_2^b)\sin(\phi_2^b))}\right]. \qquad (8)
\end{aligned}$$

In the most influential case when the AoAs of two users completely share the same common scatters ($\theta_1^b = \theta_2^b$) and ($\phi_1^b = \phi_2^b$), the right hand side of (8) is equal to

$$\frac{1}{N_b}[N_{b_x}][N_{b_y}] = \frac{1}{N_b}[N_b] = 1.$$

Importantly, this extreme case means that we cannot differentiate the signals from different users by constructing an array response since they share the same AoAs. Thus the key concept of beamforming in hybrid D-A massive MIMO for the mm-Wave system is not practically useful in the system any more. The resulting array response of this case is shown in Fig.5 (a). Note that, in Fig. 5, the system parameters are set as $K = 2$ and $N_r = 16$, so there should be two main spatial beams along with their own side lobes. It can be observed from Fig. 5(a) that it is impossible to distinguish between the two users' spatial beams, from the top view of the BS.

Interestingly, in the most likely case where ($\theta_1^b \neq \theta_2^b$) and ($\phi_1^b = \phi_2^b$), or ($\theta_1^b = \theta_2^b$) and ($\phi_1^b \neq \phi_2^b$), the right hand side of (8) is equal to

$$\frac{1}{N_b}[N_{b_y}]\left[\frac{1-e^{jkdn_{b_x}(\sin(\theta_1^b)\sin(\phi_1^b)-\sin(\theta_2^b)\sin(\phi_2^b))}}{1-e^{jkd(\sin(\theta_1^b)\sin(\phi_1^b)-\sin(\theta_2^b)\sin(\phi_2^b))}}\right]=\frac{1}{N_{b_x}}v_2(\theta_1^b,\phi_1^b,\theta_2^b,\phi_2^b).$$

The array response in this case is shown in Fig. 5 (b). It is seen from Fig. 5(b) that a spatial beam with its own side lobes can be detected by the receiver in Fig. 3(b) when either the zenith or azimuth AoAs do not share common scatters. For the last case where ($\phi_1^b \neq \phi_2^b$) and ($\theta_1^b \neq \theta_2^b$), again we take the right hand side of (8) which gives

$$\begin{aligned}
&\frac{1}{N_b}\left[\frac{1-e^{jkdn_{b_y}(\cos(\phi_1^b)-\cos(\phi_2^b)}}{1-e^{jkd(\cos(\phi_1^b)-\cos(\phi_2^b)}}\right]\\
&\qquad\times\left[\frac{1-e^{jkdn_{b_x}(\sin(\theta_1^b)\sin(\phi_1^b)-\sin(\theta_2^b)\sin(\phi_2^b))}}{1-e^{jkd(\sin(\theta_1^b)\sin(\phi_1^b)-\sin(\theta_2^b)\sin(\phi_2^b))}}\right]\\
&\qquad=\frac{1}{N_b}v_1(\phi_1,\phi_2)v_2(\theta_1^b,\phi_1^b,\theta_2^b,\phi_2^b).
\end{aligned}$$

Fig. 5(c) shows the case when AoAs of different users from side and top views are well separated ($\theta_1^b \neq \theta_2^b$) and ($\phi_1^b \neq \phi_2^b$), i.e., the users do not share any common scatterers, which allows them to align their beams in a specific direction.

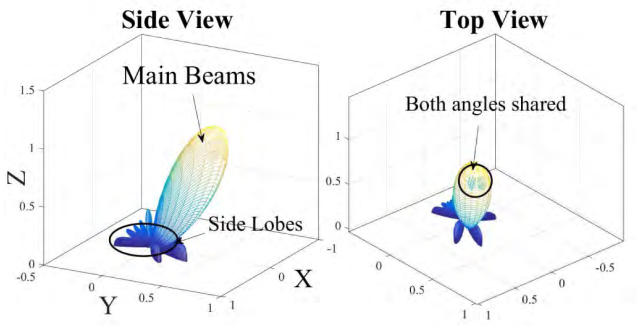

(a) Case1: Fully overlapped AoAs where $(\theta_1^b = \theta_2^b)$ and $(\phi_1^b = \phi_2^b)$.

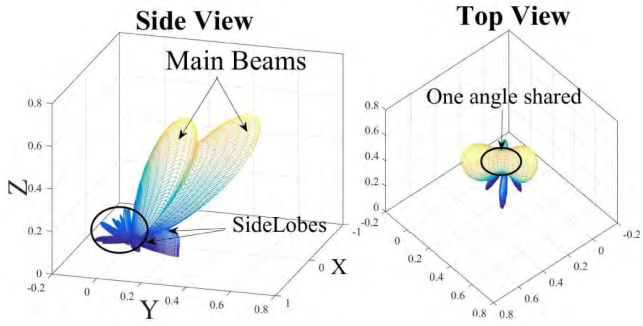

(b) Case2: Partially overlapped AoAs where $(\theta_1^b \neq \theta_2^b)$ and $(\phi_1^b = \phi_2^b)$, or $(\theta_1^b = \theta_2^b)$ and $(\phi_1^b \neq \phi_2^b)$.

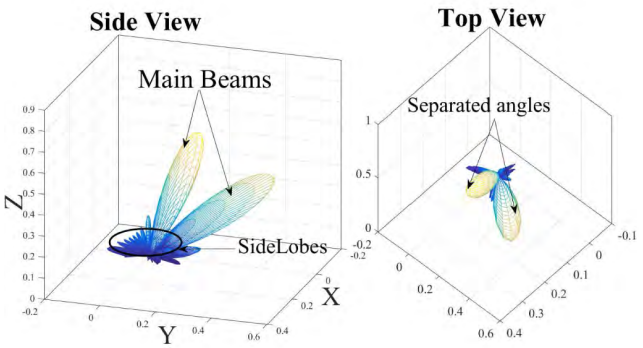

(c) Case3: Non-overlapped AoAs where $(\theta_1^b \neq \theta_2^b)$ and $(\phi_1^b \neq \phi_2^b)$.

FIGURE 5. Propagation wave shape (beampattern) by applying different cases of AoAs.

Lemma 1 shows that the multi-user hybrid D-A massive MIMO mm-Wave system can easily lose its effectiveness in applying the beamforming technique for transmission when the propagation signals (waves) of different users pass through common scatters.

In the existing proposed multiuser hybrid D-A massive MIMO [9]–[12] it is assumed that a large number of antennas is implemented, and the channel vector of a desired user will tend to be independent or more asymptotically orthogonal to the channel vector of a randomly selected interfering user. However, in industry environments as shown in

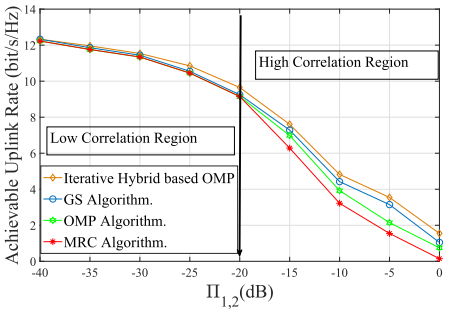

FIGURE 6. Achievable uplink rate versus correlation between two users.

Section II-B, when different users transmit through common scattering environments the channel vectors for different users are correlated, or not asymptotically orthogonal any more [24]. Intuitively, the correlation between the channel vectors of different users in a mm-Wave system defined in (9), is a good method to measure the orthogonality of these channel vectors. The correlation $\Pi_{i,k}$ of the magnitude of the inner product between the channel vectors is defined as

$$\Pi_{i,k} \triangleq \frac{|\boldsymbol{sv}_b^H(\theta_i^b, \phi_i^b)\boldsymbol{sv}_b(\theta_k^b, \phi_k^b)|}{||\boldsymbol{sv}_b(\theta_i^b, \phi_i^b)||_2||\boldsymbol{sv}_b(\theta_k^b, \phi_k^b)||_2}. \tag{9}$$

To show its impact on the achievable uplink rate, a simulation result is formed between two users in Fig. 6. The conventional algorithms iterative hybrid based on OMP [18], GS [17], OMP [12] and MRC [11] based on hybrid D-A massive MIMO mm-Wave systems is applied in this result at SNR=−10 dB. The channel parameters are set as 12 scatters, 4 clusters and $L_{km} = 3$, also the BS is equipped with $N_{RF} = K = 2, N_r = 128$, and each user is built with $N_t = 16$. Importantly, it is seen that all the algorithms lose their performance sharply when there is a high correlation between the channel vectors of the two users especially for correlations larger than −20 dB. In other words, most propagation paths of the measured users share most of the common scatters in the channel which arrive with highly overlapped AoAs at the BS. However, in a low correlation when the propagation paths do not share common scatters, all the algorithms achieve a similar and high achievable uplink rate. Therefore, theoretically there is one, low correlation region and one high correlation region. As our main goal in this paper is to maximize the achievable uplink rate in the common scattering environment, the high correlation region is our target when designing the precoders and combiners for the hybrid D-A system.

Our work contrasts the common assumption that a large number of antennas can always provide independent channel vectors regardless of the environment for multi-user hybrid D-A massive MIMO mm-Wave systems.

III. PROBLEM FORMULATION

For the industrial scenarios, multiple users transmit their signals through common scatters, resulting in interference at the BS due to overlapped AoAs is considered in this paper. This problem constitutes a challenge that exhausts the

achievable uplink rate of multi-user hybrid D-A massive MIMO mm-Wave systems.

To mitigate the risk of this problem, previously a null space method solution has been proposed in [25], principally based on capturing the desired user paths from the interfering paths while requiring the fully digital system. The role of this solution is based on the assumption that the orthogonal signal subspaces can be derived from the covariance matrix $\boldsymbol{R}$, where $\boldsymbol{R}$ is obtained separately from the desired and interference channels. This provides the ability to abstract the desired signal from the interfering signals by making all the paths from different users fall into the null space of its covariance matrix. Consequently, an ideal case is assumed that, *the possibility of different propagation paths to have overlapped AoAs at the BS is almost zero*. This result is rooted in the law of the fully digital system, because such a solution needs to be spatially applied in the system which requires that the number of RF chains equals the number of antennas. However, this method is impossible to be directly applied to hybrid D-A massive MIMO mm-Wave systems, as fewer RF chains are utilized in the system. It is also commonly suggested that the BS is always situated at a high location, and the AoA spread of different user paths that impinges at the BS are well separated, but this is not the case in industrial scenarios, short distance propagation i.e. mm-Wave channels [1], [3].

In contrast to the literature, our proposed approach to find the hybrid D-A precoders and combiners aims to maximize the achievable uplink rate and eliminate interference due to the same AoAs of the multi-user hybrid D-A massive MIMO mm-Wave system directly. The achievable uplink rate of the system is given by

$$R^{UL} = \sum_{k=1}^{K} \log(1 + \mathrm{SINR}_k), \tag{10}$$

where SINR_k is the signal-to-interference-plus-noise ratio (SINR) of the user k which is presented as

$$\mathrm{SINR}_k = \frac{|\boldsymbol{g}_k^H \boldsymbol{H}_k \boldsymbol{j}_{RF_k}|^2}{\sum\limits_{i=1, i\neq k}^{K} |\boldsymbol{g}_k^H \boldsymbol{H}_i \boldsymbol{j}_{RF_i}|^2 + \sigma^2 ||\boldsymbol{g}_k||_2^2}. \tag{11}$$

Our prime target is to maximize the achievable uplink rate of the hybrid D-A precoding and combining system and simultaneously reduce the system interferences that are combinationally generated from overlapped AoAs problems and multi-streams transmission data at the BS. To accomplish our target, we optimize the analog precoder $\boldsymbol{j}_{RF_k}$, combiner $\boldsymbol{A}$, and the digital combiner $\boldsymbol{d}_k$. Therefore, the optimization problem is formulated as

$$R^{UL} = \max_{\{\boldsymbol{j}_{RF_k}, \boldsymbol{A}, \boldsymbol{d}_k\}} \sum_{k=1}^{K} \log(1 + \mathrm{SINR}_k), \tag{12a}$$

$$\text{s.t. } |(\boldsymbol{j}_{RF})_{n_t}| = 1, \quad \forall n_t, \tag{12b}$$

$$|(\boldsymbol{A})_{n_r, n_{RF}}| = 1, \quad \forall n_r, \ \forall n_{RF}, \tag{12c}$$

where the first and second constraints in (12b), and (12c), are subjected to the non-convex constant modulus constraints, restricting all the non-zero elements to have the same amplitude in the analog domain of the user and BS sides. Unfortunately, this makes Problem (12a) less tractable. Practically, harvesting the potential gain of nulling the overlapped AoAs interference in the analog beamformers, aids to reduce the quantization noise. This concurrently relieves the degrees of freedom necessity at the digital combiner and thus technically decreases the required number of RF chains in the hybrid D-A system. In this situation, the analog beamformers need to be precisely designed to alleviate interference due to comparable AoAs as much as possible, as well as correspondingly adjust the analog precoder.

In the following section, the analog and digital precoders and combiners are designed for multi-user hybrid D-A massive MIMO mm-Wave systems for attaining the target of the optimization Problem (12a).

IV. PROPOSED HYBRID D-A PRECODER AND COMBINER

The aim is to design hybrid D-A schemes that help in maximizing the effective gain for a particular user and concurrently reducing the system interference in both the analog and digital precoders and combiners. The analog precoder $\boldsymbol{j}_{RF_k}$ for each user k is designed based on knowledge of $\boldsymbol{H}_k$, and then the analog combiner $\boldsymbol{A}$ is designed at the BS. The effective uplink analog channel coefficients between the receiver and transmitter are collected in a consolidated matrix that is denoted as $\boldsymbol{H}^{EF}$. All the analog precoder vectors are combined in a matrix as $\boldsymbol{J} = \mathrm{diag}[\boldsymbol{j}_{RF_1}, \boldsymbol{j}_{RF_2}, \ldots, \boldsymbol{j}_{RF_K}]$. Then, the channel of each user in a matrix is represented as $\boldsymbol{H} = [\boldsymbol{H}_1^T, \boldsymbol{H}_2^T, \ldots, \boldsymbol{H}_K^T]^T$, thus $\boldsymbol{H}^{EF}$ is expressed as

$$\boldsymbol{H}^{EF} = \boldsymbol{A}^H \boldsymbol{H} \boldsymbol{J}. \tag{13}$$

The diagonal entries of $\boldsymbol{H}^{EF}$ denote the desired effective uplink analog channel gains, whereas the off-diagonal entries consist of the analog interference due to the same AoAs and also the digital multi-stream interference, which is shown as

$$\boldsymbol{H}^{EF} = \begin{bmatrix} \boldsymbol{a}_1^H \boldsymbol{H}_1 \boldsymbol{j}_1 & \boldsymbol{a}_1^H \boldsymbol{H}_2 \boldsymbol{j}_2 & \cdots & \boldsymbol{a}_1^H \boldsymbol{H}_k \boldsymbol{j}_{RF_k} \\ \boldsymbol{a}_2^H \boldsymbol{H}_1 \boldsymbol{j}_1 & \boldsymbol{a}_2^H \boldsymbol{H}_2 \boldsymbol{j}_2 & \cdots & \boldsymbol{a}_2^H \boldsymbol{H}_k \boldsymbol{j}_{RF_k} \\ \vdots & \vdots & \ddots & \vdots \\ \boldsymbol{a}_{N_{RF}}^H \boldsymbol{H}_1 \boldsymbol{j}_1 & \boldsymbol{a}_{N_{RF}}^H \boldsymbol{H}_2 \boldsymbol{j}_2 & \cdots & \boldsymbol{a}_{N_{RF}}^H \boldsymbol{H}_k \boldsymbol{j}_{RF_k} \end{bmatrix}$$

For this reason, in what follows, the designing of the analog precoders and combiners must be precise, initially maximizing the diagonal elements of $\boldsymbol{H}^{EF}$, then sequentially vanishing the off-diagonal elements. Importantly, the digital combiner will be designed such to further decrease the off-diagonal entries effects. The k-th diagonal term of $\boldsymbol{H}^{EF}$ is represented as

$$\boldsymbol{H}^{EF}(N_{RF}, k) = \boldsymbol{a}_{N_{RF}}^H \boldsymbol{H}_k \boldsymbol{j}_{RF_k}. \tag{14}$$

Note here, the analog precoder and combiner are designed in the system separately, to reduce the complexity of the system and also evade any extra information that can be

exchanged between the receiver and transmitter. The proposed framework of the steps and algorithms that enhance the received signal-to-noise ratios (SNR) as well as nulling the interference consists of three key steps, discussed in detail in the following subsection. Firstly, the analog beamformers $\boldsymbol{j}_{RF_k}$ and $\boldsymbol{A}$ are designed under non-convex constant modulus constraints (12b) and (12c), respectively, for each user intending to maximize particularly the corresponding effective uplink analog channel gains. Secondly, to tractably mitigate the interference from the same AoAs, PI is proposed for forming the analog precoder, followed by a ROSt method under orthogonal constraints to design the analog combiner. Thirdly, to further diminish the effect of the interference in the system, an MMSE solution is adopted which aims to design the digital combiner based on the effective uplink analog channel gains.

A. ANALOG PRECODER DESIGN

As defined previously, $\boldsymbol{j}_{RF_k}$ is the analog precoder of each user k which is implemented by phase-only. To exploit the potential gains that each user possesses in its channel $\boldsymbol{H}_k$, a PI algorithm is proposed to calculate only the eigenvector that corresponds to the largest eigenvalue of a matrix. This algorithm involves multiplying the diagonalized matrix by a randomly chosen vector, and iteratively normalizing and multiplying the matrix by the normalized vector from the previous step. After efficiently computing the largest eigenvalue and denoting the corresponding eigenvector of a diagonalizable matrix, we then extract the phase of the eigenvector that is corresponding to the largest eigenvalue to precisely create the analog precoder $\boldsymbol{j}_{RF_k}$ at each user. Suppose $\boldsymbol{P} = \boldsymbol{H}_k^H \boldsymbol{H}_k$ where $\boldsymbol{P} \in \mathbb{C}^{N_t \times N_t}$, is Hermitian and a diagonalizable matrix. In linear algebra, a square matrix $\boldsymbol{P}$ is called diagonalizable if it is similar to a diagonal matrix i.e., if there exists an invertible matrix of $\boldsymbol{P}$ that is diagonal [26], [27]. Therefore, $\boldsymbol{P}$ consists of N_t linear independent eigenvectors $\boldsymbol{u}_1, \boldsymbol{u}_2, \ldots, \boldsymbol{u}_{N_t}$ where $\boldsymbol{u}_{N_t} \in \mathbb{C}^{N_t \times 1}$ with corresponding eigenvalues of $\gamma_1, \gamma_2, \ldots, \gamma_{N_t}$, such that $\boldsymbol{P}\boldsymbol{u}_e = \gamma_e \boldsymbol{u}_e$ for $e = 1, \ldots, N_t$. For the convergence analysis, those eigenvalues are organized in a way that $|\gamma_1| \geq |\gamma_2| \geq \cdots \geq |\gamma_{N_t}|$, where γ_1 is the dominant eigenvalue with a corresponding eigenvector of $\boldsymbol{u}_1$. In PI, suppose that a random given vector $\boldsymbol{v}^0 \in \mathbb{C}^{N_t \times 1}$ is an approximation to an eigenvector of $\boldsymbol{P}$ with $||\boldsymbol{v}^0|| = 1$ and ${\boldsymbol{v}^0}^H \boldsymbol{u}_1 \neq 0$, continually multiply by $\boldsymbol{P}$, producing a sequence of vectors $\boldsymbol{v}^1, \boldsymbol{v}^2, \cdots$ defined as

$$\boldsymbol{v}^{\alpha} = \boldsymbol{P}\boldsymbol{v}^{(\alpha-1)} = \boldsymbol{P}^{\alpha}\boldsymbol{v}^0, \tag{15}$$

where $\alpha = 1, 2, \cdots$ is denoted as the number of iterations. As $\boldsymbol{P}$ is a diagonalizable matrix, each vector is a linear combination of the eigenvectors which is represented as

$$\boldsymbol{v}^0 = c_1\boldsymbol{u}_1 + c_2\boldsymbol{u}_2 + \cdots + c_{N_t}\boldsymbol{u}_{N_t}, \tag{16}$$

where $c_1 \neq 0$ is a normalizing constant

$$\begin{aligned}
\boldsymbol{v}^1 &= \boldsymbol{P}\boldsymbol{v}^0 = c_1\boldsymbol{P}\boldsymbol{u}_1 + \cdots + c_{N_t}\boldsymbol{P}\boldsymbol{u}_{N_t} \\
&= c_1\gamma_1\boldsymbol{u}_1 + \cdots + c_{N_t}\gamma_{N_t}\boldsymbol{u}_{N_t} \\
&= \gamma_1\left[c_1\boldsymbol{u}_1 + \left(\frac{\gamma_2}{\gamma_1}\right)c_2\boldsymbol{u}_2 + \cdots + \left(\frac{\gamma_{N_t}}{\gamma_1}\right)c_{N_t}\boldsymbol{u}_{N_t}\right] \\
\boldsymbol{v}^2 &= \boldsymbol{P}^2\boldsymbol{v}^1 \\
&= \gamma_1^2\left[c_1\boldsymbol{u}_1 + \left(\frac{\gamma_2}{\gamma_1}\right)^2 c_2\boldsymbol{u}_2 + \cdots + \left(\frac{\gamma_{N_t}}{\gamma_1}\right)^2 c_{N_t}\boldsymbol{u}_{N_t}\right] \\
&\vdots \\
\boldsymbol{v}^{\alpha} &= \boldsymbol{P}^{\alpha}\boldsymbol{v}^{\alpha-1} \\
&= \gamma_1^{\alpha}\left[c_1\boldsymbol{u}_1 + \left(\frac{\gamma_2}{\gamma_1}\right)^{\alpha} c_2\boldsymbol{u}_2 + \cdots + \left(\frac{\gamma_{N_t}}{\gamma_1}\right)^{\alpha} c_{N_t}\boldsymbol{u}_{N_t}\right].
\end{aligned} \tag{17}$$

As $|\gamma_1| \geq |\gamma_e|$ for $e = 2, \ldots, N_t$, it follows that the coefficients of $\boldsymbol{u}_e$ where $e = 2, \ldots, N_t$, converge to zero as $\alpha \to \infty$. Therefore, as α increases the vector $\boldsymbol{P}^{\alpha}\boldsymbol{v}^0$ develops an increasingly significant component in the direction of converging eigenvector $\boldsymbol{u}_1$. In PI, the accuracy of an approximate eigenpair $\boldsymbol{v}^{\alpha}, \gamma^{\alpha}$, is to compute the norm of the so called residual vector

$$\boldsymbol{r} = \boldsymbol{P}\boldsymbol{v}^{\alpha} - \gamma^{\alpha}\boldsymbol{v}^{\alpha}. \tag{18}$$

Furthermore, the stopping criterion in PI is introduced as

$$|\gamma^{\alpha} - \gamma^{\alpha-1}| \leqslant ||\boldsymbol{r}||_2. \tag{19}$$

Note here, that when at the first stage $\boldsymbol{v}^0$ is to the initial vector $\boldsymbol{u}_1$ from matrix $\boldsymbol{P}$, this algorithm does not converge to an exact solution. To avoid this limitation, in this paper an extra initial step is proposed for helping PI to not iterate infinitely. The angle $\angle(\boldsymbol{v}^0, \boldsymbol{u}_1)$ between the initial vector $\boldsymbol{u}_1$ and $\boldsymbol{v}^0$ is defined by a relation

$$\cos\angle(\boldsymbol{v}^0, \boldsymbol{u}_1) = \frac{{\boldsymbol{v}^0}^H \boldsymbol{u}_1}{||\boldsymbol{v}^0||_2 ||\boldsymbol{u}_1||_2}.$$

Now, if the initializing vector $\boldsymbol{v}^0$ and the vector $\boldsymbol{u}_1$ from the initial known matrix $\boldsymbol{P}$ in the first stage are perpendicular to each other, which means $\cos\angle(\boldsymbol{v}^0, \boldsymbol{u}_1) = 0$, then the next order is to re-generate a new $\boldsymbol{v}^0$, and repeat the same step. On the other hand, when $\cos\angle(\boldsymbol{v}^0, \boldsymbol{u}_1) \neq 0$, this will trigger the scheme to start and find the largest eigenvalue with a corresponding eigenvector. The normalization step is defined as

$$\boldsymbol{v}^{\alpha+1} = \frac{\boldsymbol{P}\boldsymbol{v}^{\alpha}}{||\boldsymbol{P}\boldsymbol{v}^{\alpha}||_2}. \tag{20}$$

After finding the eigenvector and eigenvalue by utilizing PI in Algorithm 1, the analog precoder $\boldsymbol{j}_{RF_k}$ is proposed as the eigenvector which corresponds to the largest eigenvalue with an element-wise normalization to satisfy the non-convex constraint (12b), of phase shifters, represented as

$$\boldsymbol{j}_{RF_k}(e) = \frac{1}{\sqrt{N_t}} e^{j \arg[\varrho_e]}, \tag{21}$$

where $\arg(x)$ generates an element containing the phase of the entries of the element x, which results in, ϱ_e is the phase of the eth element in $\boldsymbol{u}_1$. Hereafter efficiently designing the optimal first part in the diagonal elements $\boldsymbol{a}_{N_{RF}}^H \boldsymbol{H}_k \boldsymbol{j}_{RF_k}$ of $\boldsymbol{H}^{EF}$, the next important step in the following subsection is

Algorithm 1 Power Iteration Based Algorithm (PI)

Input $\boldsymbol{v}^0, \boldsymbol{H}_k\boldsymbol{P}_k, \boldsymbol{u}_k, k = 1, \ldots, K,$
Output $\boldsymbol{j}_{RF_k}$
Initialize a starting vector randomly with $||\boldsymbol{v}^0|| = 1$ and $\boldsymbol{v}^{0H}\boldsymbol{u}_1 \neq 0$;
if $\cos\angle(\boldsymbol{v}^0, \boldsymbol{u}_1) = 0$ **then**
  go back to the first step;
else if $\cos\angle(\boldsymbol{v}^0, \boldsymbol{u}_1) \neq 0$ **then**
  go to the next step;
end if
for $\alpha = 1, 2, \cdots$ **do**
  $\alpha = \alpha + 1$;
  $\boldsymbol{v}^{\alpha} = \boldsymbol{P}\boldsymbol{v}^{(\alpha-1)}$;
  $\mu_{\alpha} = ||\boldsymbol{P}\boldsymbol{v}^{\alpha-1}||_2$;
  $\boldsymbol{v}^{\alpha} = \boldsymbol{v}^{\alpha}/\mu_{\alpha}$;
  $\gamma^{\alpha} = \boldsymbol{v}^{\alpha H}\boldsymbol{P}\boldsymbol{v}^{\alpha}$
  if $|\gamma^{\alpha} - \gamma^{\alpha-1}| \leqslant ||\boldsymbol{r}||_2$, **then** stop
end for.

to design the analog combiner in order to shed further light on the significance of maximizing the diagonal elements while handling interference of off-diagonal elements of $\boldsymbol{H}^{EF}$.

B. ANALOG COMBINER DESIGN

In this subsection, the essential challenge is to design the analog combiner that simultaneously satisfies the non-convex constraint (12c), assisting to maximize the diagonal of $\boldsymbol{H}^{EF}$ and to actively reduce the off-diagonal elements that represents the interference of the system. Unfortunately, the constraint (12c) in Problem (12a) is non-convex which can result in a high computational complexity to the system to solve since it cannot be relaxed directly. Therefore, a novel efficient method to deal with this constraint is to convert it into an additional unitary condition such that $\boldsymbol{W}^H\boldsymbol{W} = \boldsymbol{I}_{N_{RF}}$. The reformulations of Problem (12a) can be expressed after replacing the analog combiner matrix $\boldsymbol{A}$ with the matrix $\boldsymbol{W} \in \mathbb{C}^{N_r \times N_{RF}}$, as

$$R^{UL} = \max_{\{\boldsymbol{A}=\boldsymbol{W}\}} \sum_{k=1}^{K} \log(1 + \mathrm{SINR}_k), \tag{22a}$$

$$\text{subject to } \boldsymbol{W}^H\boldsymbol{W} = \boldsymbol{I}_{N_{RF}}, \tag{22b}$$

where $\boldsymbol{W}$ is the matrix that needs to be optimized. Note here, the constraint (12b) is not imposed in Problem (22a), because it is satisfied in the previous Section III-A. The constraint set $\boldsymbol{W}^H\boldsymbol{W} = \boldsymbol{I}_{N_{RF}}$ is a submanifold of $\mathbb{C}^{N_r \times N_{RF}}$ called the Stiefel manifold. The optimization Problem (22a) is defined over a novel ROSt based on the Stiefel manifold which is of interest in the study of geometry, topology, and analysis [28], [29]. The standard notation of the Stiefel manifold is $\mathcal{S}_{N_{RF}}^{N_r}$. The reason for selecting the (compact) Stiefel manifold is that it is the Riemannian submanifold of orthogonal matrices [28], [29]. Therefore, we only use the orthogonal Stiefel manifold matrices $\boldsymbol{W} \in \mathcal{S}_{N_{RF}}^{N_r}$ to represent subspaces. An optimal $\boldsymbol{W}$ is required to be selected in the tangent plane of the Stiefel manifold which can maximize the cost function. The feasible set of Stiefel manifolds $\mathcal{S}_{N_{RF}}^{N_r}$ is represented as $\mathcal{S}_{N_{RF}}^{N_r} = \left\{\boldsymbol{W} \in \mathbb{C}^{N_r \times N_{RF}}, \boldsymbol{W}^H\boldsymbol{W} = \boldsymbol{I}_{N_{RF}}\right\}$. Algorithm 2 based on ROSt with three stages in each iteration is proposed to find the optimal $\boldsymbol{W}$; 1) the tangent space refinement; 2) Riemannian gradient; 3) retraction.

Step-1 Tangent Space Refinement of a Manifold Structure: The ROSt based on Stiefel manifold admits a tangent space at each point. Each point $\boldsymbol{W}$ in an embedded sub-manifold has a tangent space which is represented by $\mathcal{T}_{\boldsymbol{W}}\mathcal{S}_{N_{RF}}^{N_r}$. The tangent space consists of a tangent vector ξ of the curves which is represented by a matrix $\boldsymbol{\xi} \in \mathbb{C}^{N_r \times N_{RF}}$, thus, the tangent space at point $\boldsymbol{W}$ can be depicted as

$$\mathcal{T}_{\boldsymbol{W}}\mathcal{S}_{N_{RF}}^{N_r} = \{\boldsymbol{\xi} \in \mathbb{C}^{N_r \times N_{RF}} : \mathbb{R}\{\boldsymbol{\xi} \odot \boldsymbol{W}^H\} = \boldsymbol{0}_{N_r \times N_{RF}}\}. \tag{23}$$

In a manifold, each tangent space is given by an inner product. In this algorithm, Riemannian metric is used as the inner product which varies smoothly from point to point and is represented as

$$\forall \boldsymbol{\xi}_1, \boldsymbol{\xi}_2 \in \mathcal{T}_{\boldsymbol{W}}\mathcal{S}_{N_{RF}}^{N_r}, \langle \boldsymbol{\xi}_1, \boldsymbol{\xi}_2 \rangle = \mathrm{trace}(\boldsymbol{\xi}_1^H\boldsymbol{\xi}_2). \tag{24}$$

Step-2 The Riemannian Gradient: the Riemannian gradient of f at point $\boldsymbol{W}$ is simply the linear projection of the ordinary gradient of f onto the tangent space. Therefore, the Riemannian gradient of the function at $\boldsymbol{W}$ is defined by computing the gradient of $\mathrm{grad}f(\boldsymbol{W})$, in the usual way, then projecting the Euclidean gradient $\nabla f(\boldsymbol{W})$ firstly onto the tangent space $\mathcal{T}_{\boldsymbol{W}}\mathcal{S}_{N_{RF}}^{N_r}$, and then to the Stiefel manifold

$$\begin{aligned}\mathrm{grad}f|_{\mathcal{S}_{N_{RF}}^{N_r}}(\boldsymbol{W}) &= \mathbf{Proj}_{\boldsymbol{W}}^{\mathcal{S}}\nabla f(\boldsymbol{W}) \\ &= (\boldsymbol{I}_{N_{RF}} - \boldsymbol{W}\boldsymbol{W}^H)\nabla f(\boldsymbol{W}),\end{aligned} \tag{25}$$

where $\nabla f(\boldsymbol{W})$ named the Euclidean gradient of (22a), which is derived in (26), as shown at the bottom of the next page, where $\boldsymbol{g}_k = \boldsymbol{W}\boldsymbol{d}_k$, in this stage only the digital combiner is assumed to be an identity matrix $\boldsymbol{I}_{N_{RF}}$.

Step-3 The Retraction: Retraction $\mathrm{R}_{\boldsymbol{W}}(\boldsymbol{\xi})$ on $\mathcal{S}_{N_{RF}}^{N_r}$ is another concept which maps every vector from a given point $\boldsymbol{W}$ along a prescribed direction $\boldsymbol{\xi}$ while remaining on the manifold, and is expressed as

$$\mathrm{R}_{\boldsymbol{W}}(\boldsymbol{\xi}) = \mathrm{polar}(\boldsymbol{W} + \boldsymbol{\xi}), \tag{27}$$

where $\mathrm{polar}(\boldsymbol{W} + \boldsymbol{\xi}) \in \mathcal{S}_{N_{RF}}^{N_r}$ designates the $N_r \times N_{RF}$ orthonormal factor of the polar decomposition of $(\boldsymbol{W} + \boldsymbol{\xi})$. For example, if $\boldsymbol{\upsilon} = (\boldsymbol{W} + \boldsymbol{\xi})$, then to compute the polar of $\boldsymbol{\upsilon}$, a thin SVD is used which means $\boldsymbol{\upsilon} = \boldsymbol{\Xi}\boldsymbol{\Sigma}\boldsymbol{\Gamma}^T$, and $\mathrm{polar}(\boldsymbol{\upsilon}) = \boldsymbol{\Xi}\boldsymbol{\Gamma}^T$. In order to guarantee that the objective function is non-decreasing at each iteration α, the Armijo backtracking line step of length ε and the Polak-Ribiere parameter [28] are defined and tracked in Algorithm 2. On manifolds, it is necessary to compare vectors belonging to different tangent spaces. Ideally, the gradient at the current iteration is combined with the search direction followed at the previous iteration. To combine them, a mathematical tool capable of computing the transport vectors [29] of the tangent vector $\boldsymbol{\xi}$ at $\boldsymbol{W}^{\alpha}$ to $\boldsymbol{W}^{\alpha+1}$ is used, which is represented as

$$\mathrm{Transp}_{\boldsymbol{W}^{\alpha} \to \boldsymbol{W}^{\alpha+1}} = (\boldsymbol{I}_{N_{RF}} - \boldsymbol{W}^{\alpha+1}(\boldsymbol{W}^{\alpha+1})^H)\nabla f(\boldsymbol{W}). \tag{28}$$

and is applied as given in step 6 of Algorithm 2 which provides the architecture of ROSt algorithm based on Stiefel

Algorithm 2 Riemannian Optimization Methods Based on Stiefel Manifold (ROSt)

Input $\boldsymbol{W}, \boldsymbol{H}_k, \boldsymbol{j}_{RF_k}, \boldsymbol{D} = I, k = 1, \ldots, K,$
Output $\boldsymbol{A}, \boldsymbol{a}_k$
Require: $\alpha = 0$ and $\boldsymbol{W}^0 \in \mathcal{S}_{N_{RF}}^{N_r}$;
$\boldsymbol{\xi}^0 = -\text{grad}f(\boldsymbol{W}^0)$
Repeat
$\varepsilon^\alpha = \text{Linesearch}(\boldsymbol{W}^\alpha, \boldsymbol{\xi}^\alpha, \boldsymbol{W}^{\alpha+1})$ ▷ Armijo backtracking step size;
$\boldsymbol{W}^{\alpha+1} = \text{R}_{\boldsymbol{W}}(\boldsymbol{\xi})$ ▷ search for the next point;
$\boldsymbol{\kappa}^{\alpha+1} = \text{grad}f(\boldsymbol{W}^{\alpha+1})$ ▷ Determine the gradient;
$(\boldsymbol{\xi}^\alpha)^+ = \text{Transp}_{\boldsymbol{W}^\alpha \to \boldsymbol{W}^{\alpha+1}}$ ▷ find the transport;
Select Polak-Ribiere $\gamma^{\alpha+1}$;
$\boldsymbol{\xi}^{\alpha+1} = -\boldsymbol{\kappa}^{\alpha+1} + \gamma^{\alpha+1}(\boldsymbol{\xi}^\alpha)^+$ ▷ the new conjugate direction;
$\alpha \leftarrow \alpha + 1$;
Until a stopping criterion triggers.

manifold optimization. To ascertain that Algorithm 2 based on the ROSt converges, suppose $\boldsymbol{W}^\alpha$ to be an infinite sequence of iterations originated by Algorithm 2 which resulting accumulation point is a critical point of the defined cost function. Therefore, in theorem 4.3.1 in [29] and section 4.1 in [30], it has been proven that the convergence on manifolds is guaranteed.

One of the main points of selecting (22a) to be the Euclidean gradient when designing $\boldsymbol{W}$ instead of only focusing on the desired user (i.e., the diagonal elements of $\boldsymbol{H}^{EF}$), is also to effectively design an optimal $\boldsymbol{W}$ that assists in keeping the off-diagonal effective uplink analog channel elements small. To clarify this conceptually, the receiver has to apply the same analog beamforming matrix to combine all K users' data. The optimal $\boldsymbol{W}$ already consists of K columns of optimal vectors $[\boldsymbol{w}_1^*, \boldsymbol{w}_2^*, \ldots, \boldsymbol{w}_K^*]$, where $\boldsymbol{w}_k \in \mathbb{C}^{N_r}$, which guarantees the fairness among all K users. Then mathematically each vector can simultaneously maximize its corresponding gain $\boldsymbol{w}_k^* = \underset{\boldsymbol{w}_k}{\text{argmax}} ||\boldsymbol{w}_k^H \boldsymbol{H}_k \boldsymbol{j}_{RF_k}||_F^2$. When different users with different effective uplink analog channel coefficients $\boldsymbol{w}_k^H \boldsymbol{H}_k \boldsymbol{j}_{RF_k}$ and $\boldsymbol{w}_i^H \boldsymbol{H}_i \boldsymbol{j}_{RF_i}$ are highly correlated, the vectors $\boldsymbol{w}_k$ and $\boldsymbol{w}_i$ in the analog domain $\boldsymbol{W}$ attain this condition $\boldsymbol{w}_k^{*H} \boldsymbol{w}_i^* \approx 0$ which can actively reduce the interference due to the correlated vectors.

So far, the obtained $\boldsymbol{W}$ from Algorithm 2 is the solution that only satisfies the orthogonal constraints (22b), but it does not satisfy the constant modulus constraint in (12c). Since matrix $\boldsymbol{W}$ has N_{RF} orthonormal columns, and matrix $\boldsymbol{A}$ needs constant modulus, i.e., $\frac{1}{\sqrt{N_r}}$, then the minimum value can be achieved when $\boldsymbol{A}$ has the same phase components as $\boldsymbol{W}$,

$$\boldsymbol{A} = \frac{1}{\sqrt{N_r}} e^{j \arg(\boldsymbol{W})}. \tag{29}$$

where $\arg(\boldsymbol{X})$ generates a matrix containing the phases of the entries of the matrix $\boldsymbol{X}$. Ideally, as all the elements in $\boldsymbol{A}$ have a constant modulus, the phases of all the elements in $\boldsymbol{A}$ are the same as the elements of the corresponding orthonormal $\boldsymbol{W}$. This point is proven by utilizing the properties of complex numbers [31]. Thus the proposed solution in (25) satisfies the constraint in (12c).

Note here, a metric is defined based on the diagonally dominant matrix condition $|\boldsymbol{H}_{k,k}^{EF}| > \sum_{i \neq 1} |\boldsymbol{H}_{k,i}^{EF}|$ [32], for illustrating the robustness of the proposed algorithms PI and ROSt. This metric is introduced as

$$\text{Ratio} = \frac{|\boldsymbol{H}_{k,k}^{EF}|}{\sum_{i \neq 1} |\boldsymbol{H}_{k,i}^{EF}|}, \tag{30}$$

where $\boldsymbol{H}_{k,k}^{EF}$ is the diagonal element in each row, and $\boldsymbol{H}_{k,i}^{EF}$ is the off-diagonal element in the same row of $\boldsymbol{H}^{EF}$, respectively. For comparison, we suppose there are three users transmitting through a common scattering scenario, where the number of RF chains equals the number of users i.e., $N_{RF} = K = 3$ and $N_t = 4$ and $N_r = 16$. Now, several $\boldsymbol{H}^{EF}$ are generated by different algorithms, the proposed methods (PI and ROSt), iterative hybrid based OMP [18], GS [17], OMP [12], and MRC [11] and their Ratios are compared in Fig. 7 in which each bar represents a row of $\boldsymbol{H}^{EF}$. It can be noticed that the diagonal entries of $\boldsymbol{H}^{EF}$ that are generated by our proposed algorithms attain higher values compared to the off-diagonal elements and, consequently, a superior Ratio is obtained. Intuitively, it can be also recognized that the off-diagonal values of the other compared algorithms are close enough to the diagonal values which affects the Ratio directly and makes it always close to one.

Ultimately, ROSt as summarized in Algorithm 2, achieves the target of designing an analog combiner $\boldsymbol{A}$ for maximizing the desired user and assisting in reducing all the off-diagonal elements effects.

C. DESIGN OF DIGITAL COMBINER

In this subsection, after having accomplished the design of the analog precoder and combiner, a next important step is the design of the digital combiner. The digital combiner is proposed based on MMSE by exploiting the effective uplink analog channel gains. For each user k, its effective uplink analog channel gains can be defined as $\bar{\boldsymbol{h}}_k = \boldsymbol{H}_k \boldsymbol{j}_{RF_k} \in \mathbb{C}^{N_r}$. Therefore, the optimal MMSE combiner, which helps in further decreasing the off-diagonal elements, is designed

$$\nabla f(\boldsymbol{W}) = \left(\frac{1}{\ln(2) \left(1 + \frac{|\boldsymbol{g}_k^H \boldsymbol{H}_k \boldsymbol{j}_{RF_k}|^2}{|\boldsymbol{g}_k^H \boldsymbol{H}_i \boldsymbol{j}_{RF_i}|^2 + \sigma^2 ||\boldsymbol{g}_k||_2^2} \right)} \cdot \frac{\boldsymbol{g}_k^H \boldsymbol{H}_k \boldsymbol{j}_{RF_k} \boldsymbol{j}_{RF_k}^H \boldsymbol{H}_k^H (|\boldsymbol{g}_k^H \boldsymbol{H}_i \boldsymbol{j}_{RF_i}|^2 + \sigma^2 ||\boldsymbol{g}_k||_2^2) - |\boldsymbol{g}_k^H \boldsymbol{H}_k \boldsymbol{j}_{RF_i}|^2 (\boldsymbol{g}_k^H \boldsymbol{H}_i \boldsymbol{j}_{RF_i} \boldsymbol{j}_{RF_i}^H \boldsymbol{H}_i^H + \sigma^2 \boldsymbol{g}_k^H)}{(|\boldsymbol{g}_k^H \boldsymbol{H}_i \boldsymbol{j}_{RF_i}|^2 + \sigma^2 ||\boldsymbol{g}_k||_2^2)^2} \right), \tag{26}$$

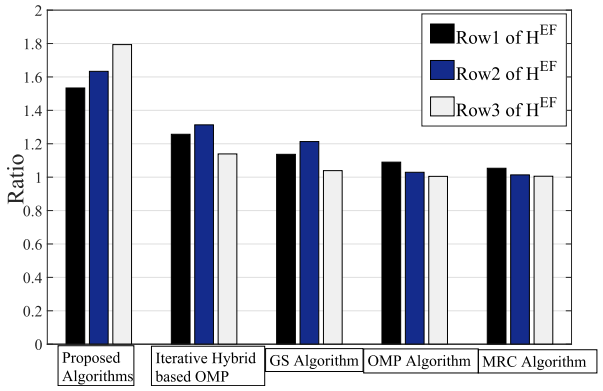

FIGURE 7. Comparison of ratios between the diagonal and off diagonal elements of $\boldsymbol{H}^{EF}$ generated by different algorithms.

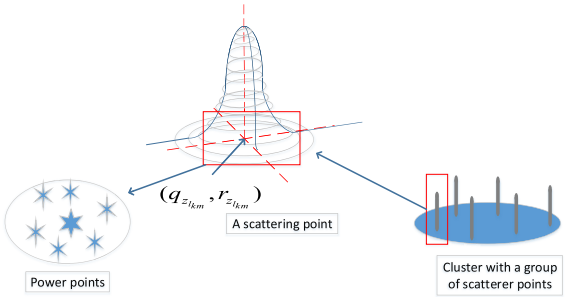

FIGURE 8. Illustration of a group of power points inside a scattering point in an industrial scenario.

as [12]

$$\boldsymbol{D} = \bar{\boldsymbol{H}}^H \boldsymbol{A}\,(\boldsymbol{A}^H \bar{\boldsymbol{H}}^H \bar{\boldsymbol{H}} \boldsymbol{A} + \frac{K\sigma^2}{\eta} \boldsymbol{A}^H \boldsymbol{A})^{-1}, \tag{31}$$

where $\bar{\boldsymbol{H}} = [\bar{\boldsymbol{h}}_1, \ldots, \bar{\boldsymbol{h}}_k]$. Ultimately, the digital combiner $\boldsymbol{D}$ that is obtained from (31) based on the effective uplink analog channel can efficiently be applied for making the off-diagonal elements have lower impact on the desired diagonal elements.

To sum up, the hybrid D-A precoders and combiners for the multi-user massive MIMO mm-Wave system in industrial scenarios were designed in a way to mitigate the system interference in both analog and digital precoders and combiners.

V. AOA ESTIMATION FOR HYBRID D-A MM-WAVE SYSTEMS

The aim of this section is to show how the proposed two-steps method can estimate the AoAs for the mm-Wave signals by exploiting the detection of the point that represents the most focused power in the scattering scenario. This power point can be represented as $(q_{z_{l_{km}}}, r_{z_{l_{km}}})$, as illustrated in Fig. 8. In [33], it has been discussed that each scattering point consists of a group of power points and that one of those power points, most probably the centre point, produces the strongest lth path as depicted in Fig. 8. The work in [33] exploited the point that has most of the power around it, to idealize the scattering function in frequency-wavenumber space in order to evaluate the performance of detectors. Specifically, this theory is proposed now as one of the main stages in estimating AoAs of mm-Wave signals. The (q,r)th component of the channel estimation matrix $[\hat{\boldsymbol{H}}_{km}]_{q,r}$ is defined in (32), as shown at the bottom of this page and it can be easily noticed that when $N_{b_x} \to \infty$ and $N_{b_y} \to \infty$, then $[\hat{\boldsymbol{H}}_{km}]_{q_{z_{l_{km}}}, r_{z_{l_{km}}}} = \sqrt{N_b} h^{3D}_{z_{l_{km}}}$ that possesses only a point where all the power will concentrate around which is represented as $(q_{z_{l_{km}}}, r_{z_{l_{km}}})$. Therefore, the estimated AoAs are formulated as

$$\begin{aligned} \hat{\theta}^b_{z_{l_{km}}} &= \arcsin\left(\lambda/d \sqrt{\left(\frac{q_{z_{l_{km}}}}{N_{b_x}}\right)^2 + \left(\frac{r_{z_{l_{km}}}}{N_{b_y}}\right)^2}\right), \\ \hat{\phi}^b_{z_{l_{km}}} &= \arctan \frac{\left(\frac{r_{z_{l_{km}}}}{N_{b_y}}\right)}{\left(\frac{q_{z_{l_{km}}}}{N_{b_x}}\right)}, \end{aligned} \tag{33}$$

where $\hat{\theta}^b_{z_{l_{km}}}$ and $\hat{\phi}^b_{z_{l_{km}}}$ are the estimated zenith and azimuth angles. For each antenna in both axes the angular domain search is represented as $\varpi^b_{z_{l_{km}}} = (n_{b_x} - 1)\frac{\pi}{\Omega}$, where $n_{b_x} = [1, \ldots, N_{b_x}]$, and $\omega^b_{z_{l_{km}}} = (n_{b_y} - 1)\frac{\pi/2}{\Omega}$, where $n_{b_y} = [1, \ldots, N_{b_y}]$. To find $\varpi^b_{z_{l_{km}}}$ and $\omega^b_{z_{l_{km}}}$ a search method called angular domain search is proposed as the second step. In this step,ranging from 0 to π and from $-\frac{\pi}{2}$ to $\frac{\pi}{2}$ are performed linearly with a step size of $\frac{\pi}{\Omega}$ and $\frac{\pi/2}{\Omega}$, where $\Omega \approx \frac{2N_b}{1.7}$ [33] is denoted as the minimum step search that relies on the number of antennas N_b employed for the AoAs search. The main concept of using such a step is to search among a range of angles and find which angle can achieve the minimum estimation error. The normalized estimation error criteria based on the estimated angles and the given channel, are applied as a performance metric E_{rr} formulated as

$$E_{rr} = 10 \log_{10}\left(\frac{\sum_{l=1}^{L_{km}} ||\bar{\boldsymbol{H}}_{km} - \boldsymbol{H}_{km}||_F^2}{\sum_{l=1}^{L_{km}} ||\boldsymbol{H}_{km}||_F^2}\right). \tag{34}$$

The zenith and azimuth angles that achieve the minimum estimation error between the estimation channel and the given channel are chosen as the estimated angles for the mm-Wave signals.

With the aforementioned criterion, we provide an estimation approach for the mm-Wave signals that suffered also from the overlapped AoAs by finding the estimated angles that constructively minimize the normalized estimation error criteria between an estimation channel and the given channel.

$$[\hat{\boldsymbol{H}}_{km}]_{q,r} = \frac{1}{\sqrt{N_b}} h^{3D}_{z_{l_{km}}} \sum_{n_{b_x}=1}^{N_{b_x}} \sum_{n_{b_y}=1}^{N_{b_y}} e^{-j(\frac{2\pi}{N_{b_x}} n_{b_x} r + \frac{2\pi}{N_{b_y}} n_{b_y} q - 2\pi d/\lambda (n_{b_y} \sin\hat{\theta}^b_{z_{l_{km}}} \cos\hat{\phi}^b_{z_{l_{km}}} + n_{b_x} \sin\hat{\theta}^b_{z_{l_{km}}} \sin\hat{\phi}^b_{z_{l_{km}}}))}. \tag{32}$$

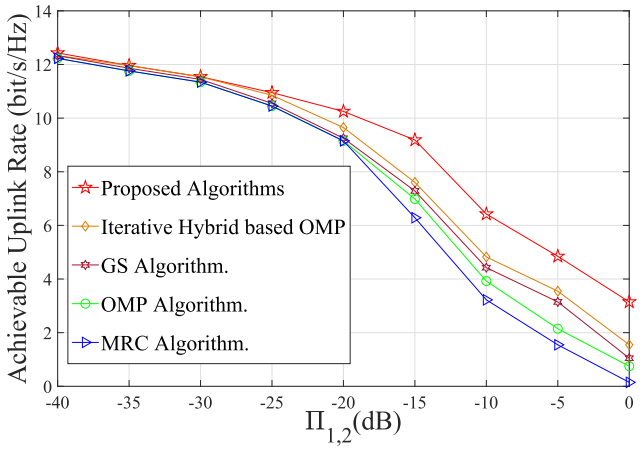

FIGURE 9. Achievable uplink rate versus channel correlation between $K = 2$ users.

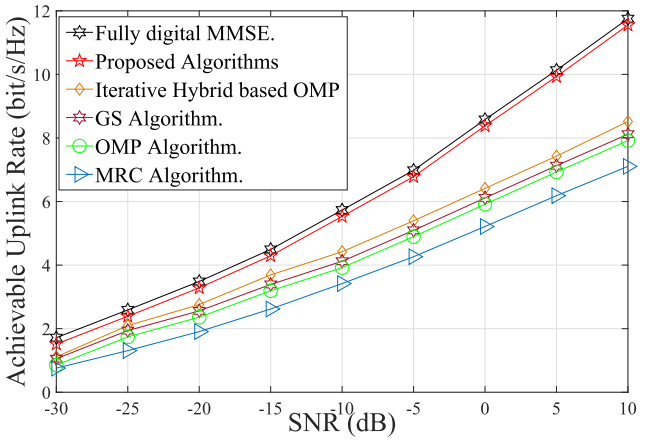

FIGURE 10. Achievable uplink rate versus SNR when $K = 2$ users and correlation $= -10$ dB.

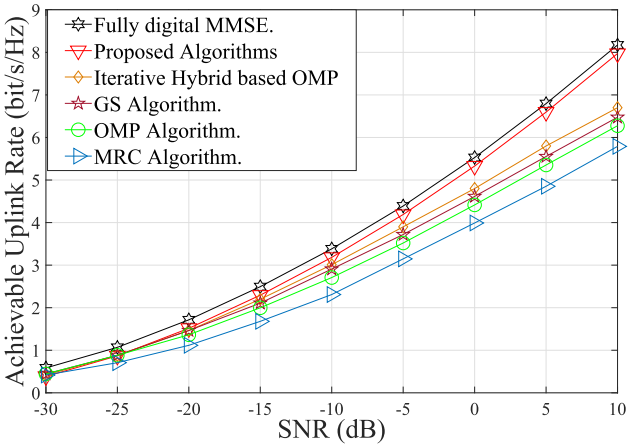

FIGURE 11. Achievable uplink rate versus SNR when $K = 2$ users and correlation $= -5$ dB.

VI. SIMULATION RESULTS

In this section, simulation results are provided to evaluate the performance of the proposed algorithms. For simplicity, the number of users equals the number of RF chains at the BS. Both BS and users are equipped with UPA, having antenna spacing $u_\delta = \frac{\lambda}{2}$, where $\delta \in [x, y]$. The mm-Wave channel as described in Section II is deployed and the number of multipaths for each user is selected randomly from $L = 3 \sim 10$ [8], [21], [34]. For all figures, the number of scatters is randomly selected between $(3 \sim 20)$ scatters with a pre-defined probability so that users share common scatters, also each scatter has unit average power. The AoAs and AoDs are generated independently from the uniform distribution with the mean cluster angle uniformly distributed over $[0, 2\pi]$, whereas the angle spread is set to 7.5 [8], [21], [34]. The BS is equipped with $N_{RF} = K = 6, N_r = 128$, and each user is built with $N_t = 16$. For fair comparison, any ZF solution in the literature algorithms is replaced by an MMSE solution.

Fig. 9 illustrates the effect of the correlation between the channel vectors of different users in a mm-Wave system on the achievable uplink rate when the SNR is set as -10 dB. There is a strong relation between the scattering environment and the orthogonality of the channel of users. It is seen that all the algorithms achieve lower performance when the correlations approach 0 dB. This shows, that when most of the propagation paths of the two users share most of the scattering points, their signals overlap at the BS, and the correlation between the channel vectors is strong which loses orthogonality. Our proposed algorithms attain a higher achievable uplink rate than the other algorithms at the practical from -20 dB until 0 dB, regime when there is a high correlation between users.

In Fig. 10 and Fig. 11, we investigate the achievable uplink rate as a function of SNR for two users, where the correlation is fixed at -10 dB and -5 dB, respectively. It can be seen that when the correlation is low at -10 dB in Fig. 10 all algorithms achieve a higher uplink rate compared to Fig. 11 when the correlation value is set as -5 dB at all SNR values. Intuitively, when the correlation of the channel vectors of these users increases due to the propagation paths sharing most of the common scattering points in the range and arrive with overlapped AoAs, the interference at the BS increases sharply which drastically reduces the performance of the system. It can be seen that the proposed algorithms are superior to the existing algorithms and perform closely to the fully digital MMSE, as the analog domain is designed directly to decrease the correlation effect resulting in a higher achievable uplink rate.

Fig. 12 displays the effect of the interference on the achievable uplink rate of hybrid D-A massive MIMO mm-Wave systems when some of the propagation paths share some common scatters. We have $K = 6$ users and the correlation between each two users is randomly selected, but within the high correlation range $(-20 \sim 0)$ dB. Further, the number of scatters is set to 12, there are 4 clusters and $L_{km} = 5$. We randomly select $(3 \sim 5)$ scatters from an existing set of scatters with a pre-defined probability that users share common scatters, also each scatter has unit average power. The fully digital MMSE system and the hybrid D-A based on iterative hybrid based OMP [18], GS [17], MRC [11] and

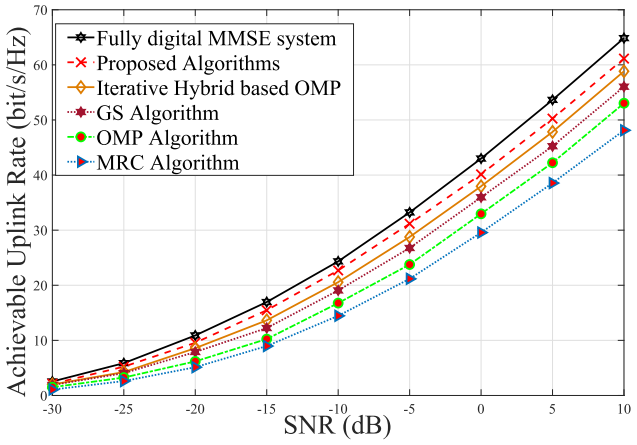

FIGURE 12. Achievable uplink rate in the overlapped AoAs scenario versus SNR, $K = 6$.

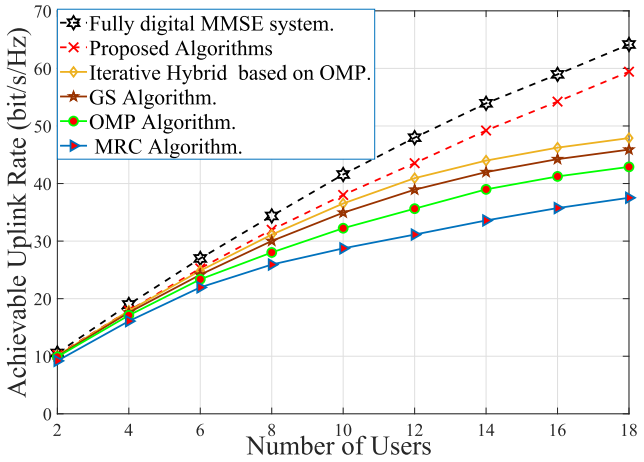

FIGURE 13. Achievable uplink rate in the overlapped AoAs scenario versus K.

OMP [12] algorithms are applied for comparison. The practical regime of the correlation between users varies from user to user in the system. For instance, when two users share most of the common scatters, then their correlation could be -6 dB, but in the case that there is no sharing between these users the correlation could be -18 dB. Noticeably, the hybrid D-A based on the proposed algorithms gain higher achievable uplink rates than the existing hybrid D-A based on iterative hybrid based OMP [18], GS [17], MRC [11] and OMP [12] algorithms, as expected. Although the iterative hybrid based OMP and GS algorithm are built to decrease the overlapped AoAs interference, they have a noticeable gap from the fully digital MMSE system, which proves that the correlation interference has not been efficiently removed. Furthermore, MRC [11] and OMP algorithms [12] have a large gap with our proposed algorithms and the fully digital MMSE, because the interference that is created due to the common scattering fades their performance improperly. Fig. 12 represents the practical scenario with users physically moving, which affects the correlation values to either increase or decrease, and our designed algorithms attain reasonable performance.

The achievable uplink rate as a function of the number of users is shown in Fig. 13. In industrial scenarios the number of users is high and varying from spot to spot which influences the users correlation values. The correlation between two users in Fig. 13 is also guaranteed to be in the high correlation range $(-20 \sim 0)$ dB at SNR $= -10$ dB. It can be observed that the achievable uplink rates of the proposed PI and ROSt algorithms significantly outperform the iterative hybrid based OMP [18], GS [17], MRC [11] and OMP [12] algorithms, especially when the number of users is large. The reason is, that as the number of users grows, more users share a small number of scatters resulting in a correlation increase between two users which generates high interference in the system. It is obvious that the iterative hybrid based OMP, and GS algorithm suffer from the high number of users, which makes both algorithm's curves bend toward the OMP curve. The existing MRC [11] and OMP [12] algorithms have not designed their hybrid D-A to reduce the effects of the interference due to common scattering in the system.

In Fig. 14, the estimation error performance as a function of the estimation channel and the given channel versus the number of antennas at the BS is illustrated. The performance of the proposed estimation method as compared to HBT improves significantly when the number of antennas increases from 10 to 20. The reason is that in our proposed estimation method the search stage can quickly improve the accuracy of the estimation channel by examining all antennas in both axes which acquires better estimation. AoA estimation in HBT suffers from the overlapped sectors problem, thus a reduced number of sectors in the space is always recommended. As a consequence, the performance of HBT for estimating the AoA will be inaccurate and having high estimation errors.

The normalized mean square error (MSE) of the estimation channel for both the proposed method and HBT is presented in Fig. 15, where the MSE is defined as $\text{MSE} = \frac{1}{K}\sum_{k=1}^{K}\frac{||\hat{\boldsymbol{H}}_{km}-\boldsymbol{H}_{km}||^2}{||\boldsymbol{H}_{km}||^2}$. The configurations in which both the transmitter and the receivers are equipped with $N_t = 8, 32$ and $N_r = 64, 128$ antennas are compared. The channel model is set as 4 clusters, 10 scatters and $L_{km} = 3$. For all number of antennas, the MSE achievements of the proposed method are superior to those of HBT. It can also be seen that by increasing the number of antennas, the MSE performance diminishes for both methods. Because the accuracy of both methods grows significantly, take SNR$=$ 16 dB as an example, the MSE of 128 antennas is around 38% better than that of 64 antennas in our proposed method.

Fig. 16 shows the convergence behavior of the ROSt algorithm and PI algorithm at 0 dB SNR. The channel model parameters are set as 4 clusters, 8 scatters and $L_{km} = 3$. The performance achieved is averaged over 10, 000 independent realizations of the channel. The curves in the figure show that the PI algorithm converges within 6 iterations, which is considerably faster than ROSt. The simple framework and

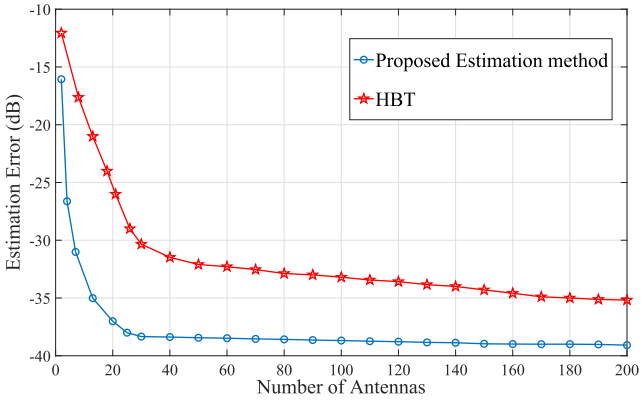

FIGURE 14. Estimation channel error performance versus the number of antennas.

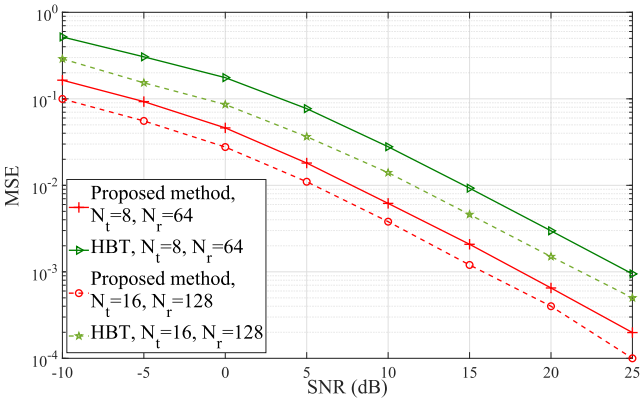

FIGURE 15. The uplink MSE performance comparison.

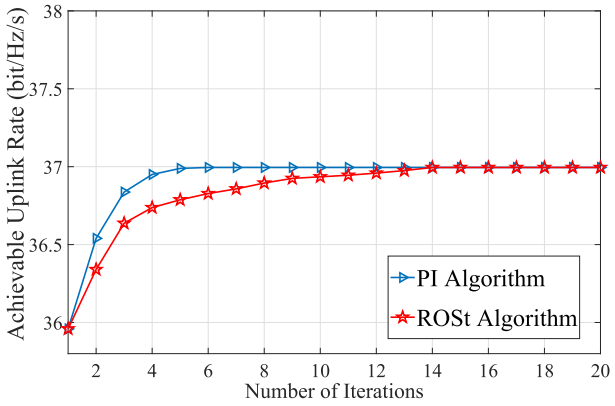

FIGURE 16. Learning curve of a our proposed algorithms.

the normalizing step of the PI algorithm actively enhance the convergence speed to reach a steady state swiftly. On the other hand, the ROSt algorithm converges within 16 iterations which is slower than the PI algorithm. The retraction step in ROSt needs more mathematical operations to pass to the next step, as was predicted in our analysis and discussions.

In Fig. 17, we consider binary phase-shift keying (BPSK) transmission to illustrate the bit-error-rate (BER)

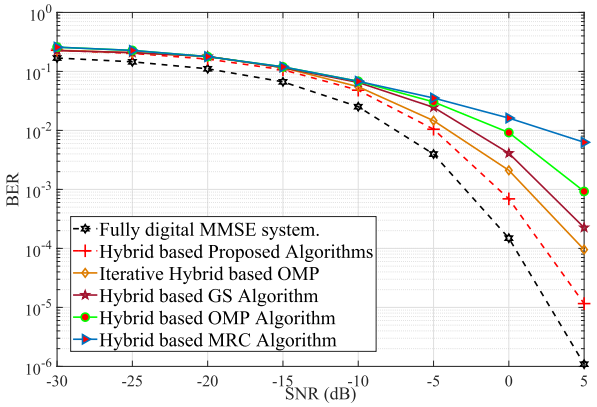

FIGURE 17. BER performance of hybrid D-A systems.

performance versus SNR when $N_{RF} = K = 4$, $N_t = 16$ and $N_r = 128$. The parameters of the channel are described as 4 clusters, 10 scatters, and $L_{km} = 3$. The proposed hybrid D-A based on ROSt and PI algorithms has a better BER performance over the hybrid D-A than the existing algorithms. These results agree with our previous analysis and simulations where our proposed algorithms have focused on eliminating the interference that are initialized due to overlapped AoAs and the multi-streams from the off-diagonal elements of $\boldsymbol{H}^{EF}$. This results in attaining a reasonable BER performance when compared with the fully digital MMSE system.

VII. CONCLUSIONS

This paper investigated the effect of the overlapped AoAs scenario on the achievable uplink rate of hybrid D-A massive MIMO mm-Wave systems in an industrial scenario. Measurements utilizing a mm-Wave system with a carrier frequency of 28 GHz have been collected in an industrial environment. Experiments show that due to the uplink signals transmitted via the common scatters, users suffer from a non-negligible interference in the system when the correlation between channel vectors increases. Hybrid D-A was proposed for the aim of maximizing the desired signal while minimizing the system interference that was generated from overlapped AoAs at the BS during simultaneous uplink transmission. Therefore, the analog part of the novel precoders and combiners was based on the reliable PI algorithm at the user and the ROSt algorithm at the BS. Then, the digital combiner was formed by applying MMSE and exploiting the effective uplink analog channel gains. Importantly, the channel estimation for hybrid D-A was examined by proposing a two-steps procedure. First, the strongest power point in each scattering point was formulated. Then, the accuracy of this procedure was actively improved by proposing a search method based on the angular domain scheme. Simulation results showed significant achievable uplink rate performance advantages of the proposed PI and ROSt algorithms, over the existing algorithms such as the iterative hybrid based OMP, GS, OMP, and MRC algorithms for overlapped AoAs scenarios. Ultimately,

the proposed estimation method attains lower error estimated channels than the recently developed HBT scheme.

REFERENCES

[1] T. S. Rappaport, G. R. Maccartney, M. K. Samimi, and S. Sun, "Wideband millimeter-wave propagation measurements and channel models for future wireless communication system design," *IEEE Trans. Commun.*, vol. 63, no. 9, pp. 3029–3056, Sep. 2015.

[2] J. Zhang, X. Ge, Q. Li, M. Guizani, and Y. Zhang, "5G millimeter-wave antenna array: Design and challenges," *IEEE Wireless Commun.*, vol. 24, no. 2, pp. 106–112, Apr. 2016.

[3] S. Le Hong Nguyen, K. Haneda, J. Jarvelainen, A. Karttunen, and J. Putkonen, "On the mutual orthogonality of millimeter-wave massive MIMO channels," in *Proc. IEEE 81st VTC Spring*, May 2015, pp. 1–5.

[4] F.-L. Luo and C. Zhang, *Massive MIMO for 5G: Theory, Implementation and Prototyping*. Hoboken, NJ, USA: Wiley, 2016.

[5] J. Wang, H. Zhu, L. Dai, N. J. Gomes, and J. Wang, "Low-complexity beam allocation for switched-beam based multiuser massive MIMO systems," *IEEE Trans. Wireless Commun.*, vol. 15, no. 12, pp. 8236–8248, Dec. 2016.

[6] M. Agiwal, A. Roy, and N. Saxena, "Next generation 5G wireless networks: A comprehensive survey," *IEEE Commun. Surveys Tuts.*, vol. 18, no. 3, pp. 1617–1655, 3rd Quart., 2016.

[7] O. El Ayach, S. Rajagopal, S. Abu-Surra, Z. Pi, and R. W. Heath, Jr., "Spatially sparse precoding in millimeter wave MIMO systems," *IEEE Trans. Wireless Commun.*, vol. 13, no. 3, pp. 1499–1513, Mar. 2014.

[8] X. Yu, J.-C. Shen, J. Zhang, and K. B. Letaief, "Alternating minimization algorithms for hybrid precoding in millimeter wave MIMO systems," *IEEE J. Sel. Topics Signal Process.*, vol. 10, no. 3, pp. 485–500, Apr. 2016.

[9] T. E. Bogale and L. B. Le, "Beamforming for multiuser massive MIMO systems: Digital versus hybrid analog-digital," in *Proc. IEEE Global Commun. Conf.*, Dec. 2014, pp. 4066–4071.

[10] A. Alkhateeb, G. Leus, and R. W. Heath, Jr., "Limited feedback hybrid precoding for multi-user millimeter wave systems," *IEEE Trans. Wireless Commun.*, vol. 14, no. 11, pp. 6481–6494, Nov. 2015.

[11] D. Ying, F. W. Vook, T. A. Thomas, and D. J. Love, "Hybrid structure in massive MIMO: Achieving large sum rate with fewer RF chains," in *Proc. ICC*, Jun. 2015, pp. 2344–2349.

[12] D. H. N. Nguyen, L. B. Le, T. Le-Ngoc, and R. W. Heath, Jr., "Hybrid MMSE precoding and combining designs for mmWave multiuser systems," *IEEE Access*, vol. 5, pp. 19167–19181, 2017.

[13] S. Hur, S. Baek, B. Kim, Y. Chang, A. F. Molisch, T. S. Rappaport, K. Haneda, and J. Park, "Proposal on millimeter-wave channel modeling for 5G cellular system," *IEEE J. Sel. Topics Signal Process.*, vol. 10, no. 3, pp. 454–469, Apr. 2016.

[14] M. K. Samimi and T. S. Rappaport, "3-D millimeter-wave statistical channel model for 5G wireless system design," *IEEE Trans. Microw. Theory Techn.*, vol. 64, no. 7, pp. 2207–2225, Jul. 2016.

[15] Y. Chen, D. Chen, Y. Tian, and T. Jiang, "Spatial lobes division-based low complexity hybrid precoding and diversity combining for mmWave IoT systems," *IEEE Internet Things J.*, vol. 6, no. 2, pp. 3228–3239, Apr. 2019.

[16] Y. Chen, D. Chen, and T. Jiang, "Non-uniform quantization codebook-based hybrid precoding to reduce feedback overhead in millimeter wave MIMO systems," *IEEE Trans. Commun.*, vol. 67, no. 4, pp. 2779–2791, Apr. 2019.

[17] J. Li, L. Xiao, X. Xu, and S. Zhou, "Robust and low complexity hybrid beamforming for uplink multiuser mmWave MIMO systems," *IEEE Commun. Lett.*, vol. 20, no. 6, pp. 1140–1143, Jun. 2016.

[18] Z. Wang, M. Li, X. Tian, and Q. Liu, "Iterative hybrid precoder and combiner design for mmwave multiuser MIMO systems," *IEEE Commun. Lett.*, vol. 21, no. 7, pp. 1581–1584, Jul. 2017.

[19] A. Alkhateeb, O. El Ayach, G. Leus, and R. W. Heath, Jr., "Channel estimation and hybrid precoding for millimeter wave cellular systems," *IEEE J. Sel. Topics Signal Process.*, vol. 8, no. 5, pp. 831–846, Oct. 2014.

[20] G. Wang, S. A. Naeimi, and G. Ascheid, "Low complexity channel estimation based on DFT for short range communication," in *Proc. IEEE ICC*, May 2017, pp. 1–7.

[21] *Study on Channel Model for Frequencies From 0.5 to 100 GHz*, 3GPP, document TS R1-155755, Oct. 2015.

[22] J. Poutanen, F. Tufvesson, K. Haneda, V. Kolmonen, and P. Vainikainen, "Multi-link MIMO channel modeling using geometry-based approach," *IEEE Trans. Antennas Propag.*, vol. 60, no. 2, pp. 587–596, Feb. 2012.

[23] E. Kampert, P. A. Jennings, and M. D. Higgins, "Investigating the V2V millimeter-wave channel near a vehicular headlight in an engine bay," *IEEE Commun. Lett.*, vol. 22, no. 7, pp. 1506–1509, Jul. 2018.

[24] H. Q. Ngo, E. G. Larsson, and T. L. Marzetta, "The multicell multiuser MIMO uplink with very large antenna arrays and a finite-dimensional channel," *IEEE Trans. Commun.*, vol. 61, no. 6, pp. 2350–2361, Jun. 2013.

[25] H. Yin, D. Gesbert, M. Filippou, and Y. Liu, "A coordinated approach to channel estimation in large-scale multiple-antenna systems," *IEEE J. Sel. Areas Commun.*, vol. 31, no. 2, pp. 264–273, Mar. 2013.

[26] T. S. Shores, *Applied Linear Algebra and Matrix Analysis*. New York, NY, USA: Springer, 2007.

[27] D. A. Harville, *Linear Models and the Relevant Distributions and Matrix Algebra*. New York, NY, USA: Springer, 2018.

[28] N. Boumal, "Optimization and estimation on manifolds," Ph.D. dissertation, Nat. Inst. Inf. Commun. Technol., Dept. Electron. Appl. Math., Univ. Catholique Louvain, Ottignies-Louvain-la-Neuve, Belgium, Tech. Rep., 2014.

[29] P.-A. Absil, R. Mahony, and R. Sepulchre, *Optimization Algorithms on Matrix Manifolds*. Princeton, NJ, USA: Princeton Univ. Press, 2008.

[30] E. Quispe and E. A. P. Quiroz, "An implementation of the steepest descent method using retractions on riemannian manifolds," Math. Optim. Soc., New York, NY, USA, Tech. Rep. 1. FCNM-UNAC 2015, 2015.

[31] G. H. Golud and C. F. Van Loan, *Matrix Computations*. Baltimore, MD, USA: The Johns Hopkins Univ. Press, 2013.

[32] F. O. Farid, "Notes on matrices with diagonally dominant properties," *Linear Algebra Appl.*, vol. 435, no. 11, pp. 2793–2812, 2011. [Online]. Available: http://www.sciencedirect.com/science/article/pii/S002437951100365X

[33] H. L. Van Trees, *Optimum Array Processing, Detection and Other Topics*. Hoboken, NJ, USA: Wiley, 2002. doi: 10.1002/0471221104.

[34] F. Sohrabi and W. Yu, "Hybrid digital and analog beamforming design for large-scale antenna arrays," *IEEE J. Sel. Topics Signal Process.*, vol. 10, no. 3, pp. 501–513, Apr. 2016.

OSAMA ALLUHAIBI received the B.E. degree in electrical and communications engineering from the University of Baghdad, Iraq, in 2006, the M.Sc. degree in electronics and communications engineering from Sam Higginbottom Institute of Agriculture, Technology and Sciences (SHUATS), India, in 2012, and the Ph.D. degree in electronics and communications engineering from the University of Kent, Canterbury, U.K., in 2018.

Since 2007, he has been with ABB Group, and also with Kalimat Telecommunication. In July 2018, he joined the Connectivity Group, WMG's Intelligent Vehicles Research Team, The University of Warwick, U.K., as a Research Fellow. His research interests include hybrid-beamforming, performance analysis of 5G millimeter-wave wireless communications systems, and 5G millimetre-wave communication for the industrial Internet of Things applications.

ERIK KAMPERT received the M.Sc. and Ph.D. degrees in natural sciences from Radboud University Nijmegen, The Netherlands, in 2005 and 2012, respectively, the latter work focusing on molecular magnetism, carried out at the High Field Magnet Laboratory and the Molecular Materials Group within the Institute for Molecules and Materials at the RU. He continued his research as a Postdoctoral Researcher with the Dresden High Magnetic Field Laboratory, Helmholtz-Zentrum Dresden-Rossendorf, Germany, where he conducted electrical transport and magnetization experiments in pulsed magnetic fields in collaboration with visiting, international scientists. In 2017, he joined the Connectivity Group, WMG's Intelligent Vehicles Research Team, The University of Warwick, U.K., as a Senior Research Fellow. Using his vast background in RF electromagnetics, the focus of his current research is on 5G millimeter-wave communication for vehicular-to-everything and the industrial Internet of Things applications.

PAUL A. JENNINGS received the B.A. degree in physics from the University of Oxford, Oxford, U.K., in 1985, and the Engineering Doctorate degree from The University of Warwick, Coventry, U.K., in 1996. From 1985 to 1988, he was a Physicist with Rank Taylor Hobson. Since 1988, he has worked on industry-focused research for the Warwick Manufacturing Group (WMG), The University of Warwick. He is currently the Deputy CTO of the WMG High Value Manufacturing Catapult Center. His current interests include vehicle electrification, particularly energy management and storage, and user engagement in product and environment design, with a particular focus on automotive and healthcare applications.

MATTHEW D. HIGGINS received the M.Eng. degree in electronic and communications engineering and the Ph.D. degree in engineering from the School of Engineering, The University of Warwick, in 2005 and 2009, respectively. Remaining at The University of Warwick, he then progressed through several Research Fellow positions, in association with some of the UKs leading defense and telecommunications companies before undertaking two years as a Senior Teaching Fellow in telecommunications, electrical engineering, and computer science subjects. In July 2012, he was promoted to the position of Assistant Professor, where his research focused on optical, nano, and molecular communications. Whilst is this position, he set up the Vehicular Communications Research Laboratory, which aimed to enhance the use of communications systems within the vehicular Space. In March 2016, he was promoted, and appointed as an Associate Professor at WMG, working in the area of connected and autonomous vehicles, where he leads the ICT and 5G themes of the group. He is a Senior Member of the FHEA, a member of the EPSRC CommNet2, and a member of the EPSRC Peer Review College.